Deanship of Graduate Studies
Al-Quds University

A COMPARATIVE STUDY OF MAGNETIC CHARACTERIZATION FOR MAGNETOCALORIC MATERIALS

Nihal Mahmoud Abd AlhamedAbuassba

M.Sc. Thesis

Jerusalem – Palestine

1446/2024

A COMPARATIVE STUDY OF MAGNETIC CHARACTERIZATION FOR MAGNETOCALORIC MATERIALS

Prepared By:

Nihal Mahmoud Abd AlhamedAbuassba

B.Sc.:Al-Quds University, Palestine

Supervisor:

Dr. Husain Alsamamra

Physics Department, Al-Quds University, Palestine

A Thesis Submitted in Partial fulfillment of requirements for the degree of Master of Science from the Department of Physics, Faculty of Science and Technology, Al-Quds University.

Jerusalem-Palestine

1446/2024

Al-Quds University

Deanship of Graduate Studies

Physics Department

Thesis Approval

A COMPARATIVE STUDY OF MAGNETIC CHARACTERIZATION FOR MAGNETOCALORIC MATERIALS

Prepared By: Nihal Mahmoud Abd Alhamed Abuassba

Registration No: 22211979

Supervisor:

Dr. Husain Alsamamra, Physics Department, Al-Quds University, Palestine.

Master thesis submitted and accepted, Date: 14-12-2024

The names and signatures of the examining committee members are as follows:

1- Head of Committee:Dr. Husain Alsamamra Signature:

2- Internal Examiner: Prof. Musa Abutier Signature:

3- External Examiner: Dr. Ishaq Musa Signature:

Jerusalem – Palestine
1446/2024

Dedication

To my father's memory, Mahmoud, to my beloved mother Faten, to my brothers Basheer, Karem, Qaiser, and Hamzeh, to my beloved sister Marah.

To my academic colleague Uday.

And to my friend and sister Haya.

Declaration

I certify that this thesis submitted for the degree of the master is the result of my research, except where otherwise acknowledged, and that this thesis, neither in whole nor in part, has been previously submitted for any degree to any other university or institution.

Signed:

Nihal Mahmoud Abd Alhamed Abuassba

Date: 14/12/2024

Acknowledgments

First and foremost, I am grateful to **Allah** for giving me the willpower, courage, and direction I needed to do this research.

I would like to express my sincere gratitude to my supervisor, **Dr. Husain Alsamamra**, for his invaluable support, encouragement, and guidance throughout this research. His extensive scientific knowledge and experience were instrumental in shaping this research.

I would also like to thank everyone who has encouraged and supported me throughout this research journey.

Abstract

The demand for an alternative to traditional refrigeration systems has grown during a period of rising energy consumption, which is predicted to triple by 2050. This is particularly true given that traditional refrigerators contribute to the ozone layer's thinning. However, research is still ongoing to obtain the best magnetic material and overcome the materials relating issues like mechanical stability, hysteresis/reversibility, or formability. This thesis presents the current trend of magnetocaloric materials and highlights the top families of compounds and alloys that have received attention in recent years. It also introduces a comparative analysis of the magnetocaloric and magnetic properties of the current trend materials ($La(Fe,Si)_{13}$, Ni_2–Mn-X-based Heusler alloys (H•A•s), and the High entropy alloys (HEAs)) according to their physical form, synthesis method, the elements of compounds and their proportions, and the effect of doping on those properties. In Ni_2MnGa, the bulk single crystal and polycrystalline bulk show good magnetocaloric properties in contrast to the microwires and nanowires. And in $La(Fe,Si)_{13}$, the melt spinning and ball milling show huge quantities of $La(Fe,Si)_{13}$ with a high purity in a very short amount of annealing time in contrast to the arc melting, which shows a large annealing time due to the slow cooling process. Also, the Curie temperature of $La(Fe,Si)_{13}$ can be increased by doping with Al or the light element H as a result of the strong exchange interaction that overcomes the kinetic energy of the itinerant electrons. In contrast to RE-free High entropy alloys, which exhibit a Curie temperature near room temperature but a small magnetic entropy change, RE-based High entropy alloys exhibit a low Curie temperature because of the weak exchange interaction and large magnetic entropy change caused by the large magnetic moments present in the rare earth elements. This study focused on the bulk properties of those MCE materials. To examine structural and magnetic properties in detail, one can use advanced techniques like X-ray absorption spectroscopy, high magnetic field measurements, and neutron scattering because they provide localized information and focus on specific atomic and magnetic environments.

Table of Contents

List of Tables

List of Figures

List of Abbreviations

MCE	Magnetocaloric effect
MCMs	Magnetocaloric materials
T_c	Curie Temperature
T_N	Néel temperature
H	Magnetic field strength
B	Magnetic flux density
M	Magnetization
Oe	Oersted
T	Tesla
Mn	Manganese
Fe	Iron
Si	Silicon
PPMS	Physical properties measurement system
VSM	Vibrating sample magnetometer
θ_{CW}	Curie-Weiss temperature
MR	Magnetic Refrigeration
FOMT	First order magnetic transition
SOMT	Second order magnetic transition
AFM	Antiferromagnetic
RCP	Relative cooling power
HEAs	High entropy alloys
XRD	X-ray diffraction
M(T)	Temperature –dependent magnetization

M(H)	Field–dependent magnetization
Ni	Nickel
Sn	Tin
Ga	Gallium
Cu	Copper
J	Joule
K	Kelvin
In	Indium
B	Boron
La	Lanthanum
FCC	Face centered cubic
BCC	Body centered cubic
Cr	Chromium
Gd	Gadolinium
Tb	Terbium
Dy	Dysprosium
Co	Cobalt
RKKY	Ruderman-Kittle-Kasuya-Yosida interaction
SOC	Spin order coupling
RE	Rare earth
Er	Erbium
Ho	Holmium
Al	Aluminum

CHAPTER ONE

INTRODUCTION AND LITERATURE SURVEY

1.1 Introduction

The magnetocaloric effect (MCE) phenomenon is a change in the temperature of magnetic material when exposed to a change of an external magnetic field (the MCE comes from magnet and calorie) **(Mezaal et al., 2017)**. One application of this phenomenon is Magnetic refrigeration (MR), although it is still under research, MR is a promising alternative to conventional refrigeration **(Law et al., 2023)**.

But as of yet, no mass-market item is offered for purchase. This is due to the fact that a number of obstacles must be overcome before magnetic refrigeration can be commercialized. It has been possible to chill homes with traditional gas-compression technology for almost a century, and currently there are about one billion of these freezers in operation. Magnetic refrigeration needs to be more economical, ecologically friendly, energy-efficient, level with traditional refrigeration, similar in weight and volume, and quieter.

1.1.1 Justifications of MCE study

- High thermodynamic efficiency and greatly outperforms traditional refrigeration in the reverse Carnot cycle.
- An environmentally friendly method that employs magnetocaloric, which has no Ozone Depleting Potential (ODP), and a heat transfer fluid unlike conventional refrigeration, which contributes to the ozone layer's thinning by using hydrofluorocarbons and chlorofluorocarbons.

- Silent and vibration-free technology: unlike conventional refrigeration, this technique does not have a compressor mechanism, which has several disadvantages such as increased noise and vibration **(Mezaal et al., 2017)**.

The adiabatic temperature change (ΔT_{ad}), the isothermal entropy change (ΔS_I), and the heat capacity (C_P) are some of the factors that affect the magnetocaloric effect. According to the relationship below equation (1.1), a material with a low heat capacity has the potential to result in a larger temperature change at the same time that the degree of freedom increases the heat capacity. For this reason, pure materials have the potential to result in larger temperature changes than intermetalic compounds and alloys because they have more degrees of freedom **(Gottschall et al., 2019)**.

$$\Delta T_{ad} \approx \frac{-T\Delta S_I}{C_P} \quad \text{.....(1.1)}$$

1.2 Overview of magnetocaloric materials

Magnetocaloric materials (MCM) are the core of magnetic refrigeration. There are two types of magnetic materials according to the order of the phase transition: first-order magnetic transition (FOMT) and second-order magnetic transition (SOMT) materials, where (FOMT) materials get a discontinuous change in magnetization (order parameter) with temperature change (control parameter), but (SOMT) materials get a continuous change in magnetization with a change in temperature **(Kitanovski, 2020)**. Regarding the magnetic field, temperature, and pressure parameters, the first-order magnetic transition exhibits a discontinuity in the first derivative of Gibbs free energy **(Pál, 1969)**, while the second-order magnetic transition is characterized by a discontinuity in the second derivative of the Gibbs free energy equation with respect to temperature, like the discontinuity in the heat capacity **(Gabbott, 2008).** Knowing the type of transition of the magnetic material is important to overcome the obstacles related to each type, according to the Ehrenfest classification, which is based on the order of discontinuity in the Gibbs potential derivative. If the first derivative of Gibbs potential, which is the magnetization M, entropy S (as in equations (1.2) and (1.3) **(Ghorai, 2022)**), and volume V, shows a discontinuity, then the type of the transition is FOMT, but the

second derivative with respect to temperature shows no discontinuity, as seen in figure 1.1 **(Lyubina, 2017)**.

$$S(T,H) = -\left(\frac{\partial G}{\partial T}\right)_H \text{.....(1.2)}$$

$$M(T,H) = -\frac{1}{\mu_0}\left(\frac{\partial G}{\partial H}\right)_T \text{.....(1.3)}$$

The phase transition concept is also associated with broken symmetry; broken symmetry occurs when the ordered ground state lacks the full symmetry of the Hamiltonian, such as the transition from paramagnetic to antiferromagnetic. The Hamiltonian describes the spin-spin interaction, and at the same time, it is invariant under rotation. The paramagnetic is also invariant under rotation, which means that when all the spins in the paramagnetic rotate by the same amount, the paramagnet's appearance will not change. Unlike the antiferromagnetic, which appears differently when rotated by an angle. As a result, an example of broken symmetry is the antiferromagnetic state **(Anderson, 1984)**.

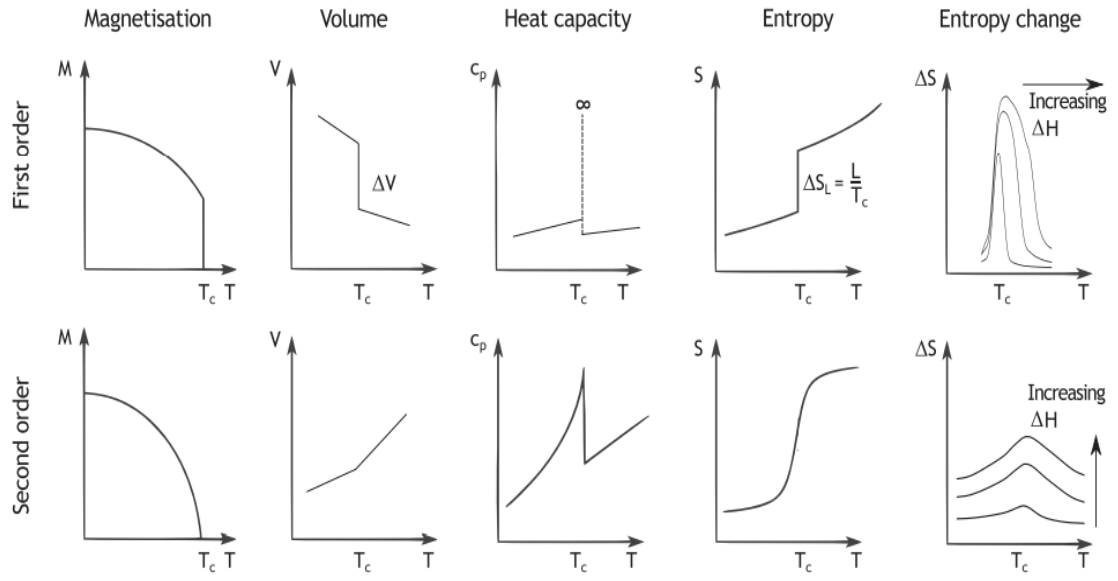

Figure 1.1 Diagram illustrating several thermodynamic parameters in dependence on the field change ΔH at first and second order magnetic phase transitions **(Lyubina, 2017)**.

Perovskite magnanites ($AMnO_3$, where A is a trivalent rare earth element) **(Ghorai, 2022),** and Gd and its alloys containing rare earth elements (such as Dy, Er, and Tb) are examples of second-order materials. However, Mn-Fe-P-Si, La-Fe-Mn-Si-H, La-Fe-Si-H, and La-Fe-Co-

Si are a few instances of first-order materials **(Kitanovski, 2020)**. FOMT materials that show a strong magnetocaloric effect called giant MCE (GMCE) **(Lyubina, 2017),** such as $Gd_5Si_2Ge_2$, which shows MCE two times than Gd, Recent research has concentrated on the FOMT as a result of the GMCE; however, investigations into SOMT continue due to its behavior at low temperatures and the advantages of non-hysteretic characteristics.

According to a literature study from the Web of Science (WoS), figure 1.2 displays the top families of magnetocaloric materials that have been published recently; their popularity (and the size of the symbol) is demonstrated by the fraction of yearly publications from 2019 to 2022. The colors of the symbols denote trends in publications: red signifies an increasing sector, blue represents a decreasing sector, and yellow (with a dashed outline) indicates stability.This thesis examines the Ni_2–Mn-X-based Heusler alloys (H•A•s) (especially for X = In or Sn), $La(Fe,Si)_{13}$ alloys, and High entropy alloys (HEAs), due to their magnetocaloric properties and the fact that they consist of abundant elements **(Law et al., 2023)**.

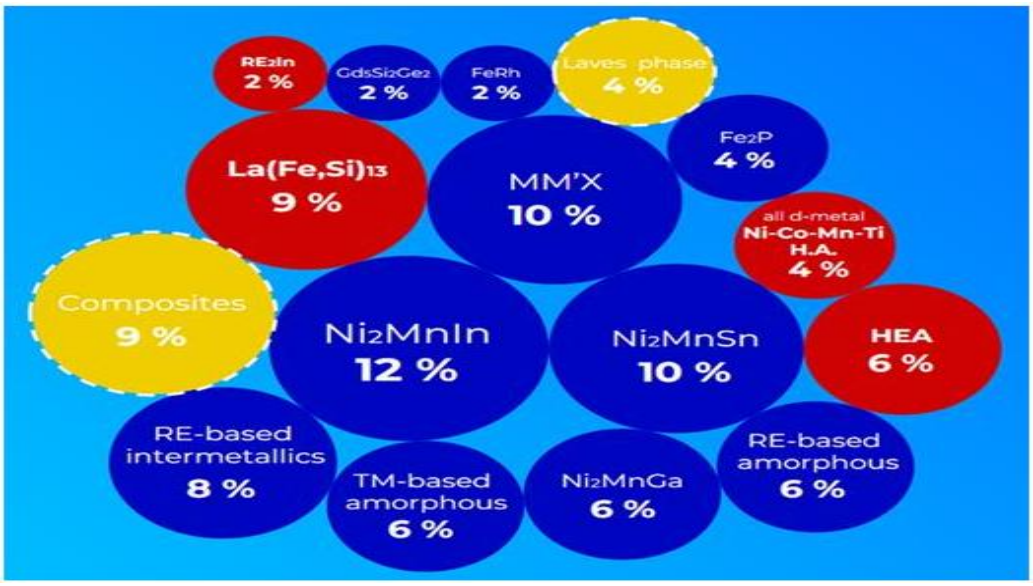

Figure 1.2 A bubble chart displaying the most popular magnetocaloric material families selected between 2019 and 2022 **(Law et al., 2023).**

Spinel ferrites with AB_2O_4, which distribute the A cations in tetrahedral sites and the B cations in octahedral sites, are a few examples of magnetocaloric materials. These materials

are characterized by minimal loss of eddy current, low synthesis costs, magnetic entropy change, and a transition temperature that can be adjusted by the type, quantity, and nature of the cations **(Oke et al., 2023)**, such as $Zn_{0.6}$ $Cu_{0.4}$ Fe_2O_4 with 305 K, 1.16 J/KgK, and 289 J/Kg at applied field 5T for Curie temperature, magnetic entropy change, and relative cooling power, respectively **(Kadiyala et al., 2018)**.

MM'X, where M, M'-metal 3d or 4d, X = main group element such as P, As, or Ge, is another kind of magnetocaloric material **(Zach et al., 2011)**, such as MnNiGe, MnCoGe, and MnCoSi with orthorhombic or hexagonal structure; another example is $Mn_{0.7}$ $Ni_{0.7}$ $Fe_{0.6}$ $Si_{0.95}$ $Al_{0.05}$ with T_c = 300 k and ΔS_m^{peak} = -19 J/KgK at applied field 5 T **(Eggert et al., 2023)**. Perovskites are also magnetocaloric materials with the chemical formula ABO_3, where A is a rare-earth or alkaline-earth element and B is a transition metal ion, such as $ErCr_{0.5}Fe_{0.5}O_3$ with ΔS_m^{peak} =12.4 J/KgK at applied field 5 T **(Yadav et al., 2020)**.

1.3 Literature Review

1.3.1 Introduction

Sometimes, researchers describe present research and development as a “new twist,” without realizing that a certain idea, concept, experiment, or study is actually many years before. Occasionally, scholars characterize current research and advancements as a “new twist” failing to acknowledge that a particular idea, concept, experiment, or study actually dates back many years **(Kitanovhski, 2020).**

The name “magnet” comes from Magnesia, a Greek province and town in Asia Minor, the literally means "the stone from Magnesia", this stone was made of natural ferric ferrite (Fe_3O_4) tones (lodestones), which was known to magnetize iron when rubbed **(Buschow & de Boer, 2003)**.

1.3.2 History of Magnetic Materials

Table (A-1.1) shows the selected years, and the main research that made a breakthrough in understanding the magnetic materials.

Year of Publication	Significant Breakthrough	References
1600	The initial individual to perform an extensive investigation of magnetism employing scientific methodologies by William Gilbert.	**(Coey & Mazaleyrat, 2023)**
1730	The first production of magnetic compound by Servington Savery.	**(Moskowitz, 1995)**
1820	Oersted established a connection between magnetism and electricity.	**(Buschow & de Boer, 2003)**
1825	Sturgeon discovered the electromagnet.	**(Buschow & de Boer, 2003)**
1880	Generated the initial hysteresis loop for iron by Warburg**.**	**(Schmool & Markó, 2018)**
1895	The relationship between the temperature and magnetization by Curie.	**(Singh, 2023)**
1905	Paul Langevin explained the theoretical framework of Paramagnetism and diamagnetism.	**(Engdahl, 2021)**
1906	The theory of ferromagnetism by Pierre Weiss.	**(Engdahl, 2021)**
1917	The reversibility of magnetocaloric effect by Auguste Picard and Pierre Weiss.	**(Weiss & Piccard, 1917)**

Table (B-1.1) shows the selected years, and the main research that made a breakthrough in understanding the magnetic materials.

1920	The physics of magnetism developed as a result of advancements in quantum mechanics.	**(Engdahl, 2021)**
1976	Brown developed an efficient refrigeration system in a room-temperature range by using gadolinium as an active material.	**(Brown, 1976)**
1997	The Giant MCE (GMCE) discovered in Gd_5 (Si_2 Ge_2) by Gschneidner and Pecharsky**.**	**(Pecharsky & Gschneidner, 1997)**
2002	Members of the Astronautics Cooperation of America created the first permanent-magnet, magnetic refrigerator at room temperature in history.	**(Klems, 2002)**

Magnetic materials play a significant role in mechanical, electromechanical, medical, and industrial devices, constituting a vital component of contemporary technology. A typical household contains around fifty devices that utilize these materials **(Buschow & de Boer, 2003)**.

The magnetocaloric effect or the material's temperature change (heating or cooling) in response to an external magnetic field, is one of the key characteristics of magnetic materials. While all magnetic materials exhibit an MCE, some materials—known as magnetocaloric materials (MCMs)—display an MCE strong enough to be employed in magnetic cooling systems **(Buschow & de Boer, 2003; Tishin & Spichkin, 2003)**.

MCE represents changes occurring in the spin structure of a magnetic material and has a significant influence on physical parameters including heat capacity, thermal conductivity, and entropy. The term "adiabatic demagnetization" was used for a while to refer to this phenomenon, which was first observed in iron approximately 143 years ago by Warburg in 1881with $T_c \approx 1043K$. The origins of the MCE were also first described by Debye in 1926

and Giauque in 1927, who proposed that a temperature lower than that of liquid helium could be reached **(Casanova i Fernàndez, 2004; Tishin & Spichkin, 2003; Mellari, 2023)**.

Researchers have been more interested in the phenomenon of MCE in recent decades as shown in figure 1.3 because of its significance in the development of magnetic cooling devices like the magnetic refrigerator, which use magnetic materials as a working body rather than gas and magnetization/demagnetization rather than compression/expansion in conventional refrigerators. On the one hand, because of the possibility of learning details about the magnetic phase and magnetic state transformations in magnetic materials that are difficult to learn through other methods. The number of studies on MCE is steadily rising in the manner described below. Nineteen articles in 1999, forty-one in 2000, ninety-one in 2001, ninety-one in 2002 **(Tishin & Spichkin, 2003)**.

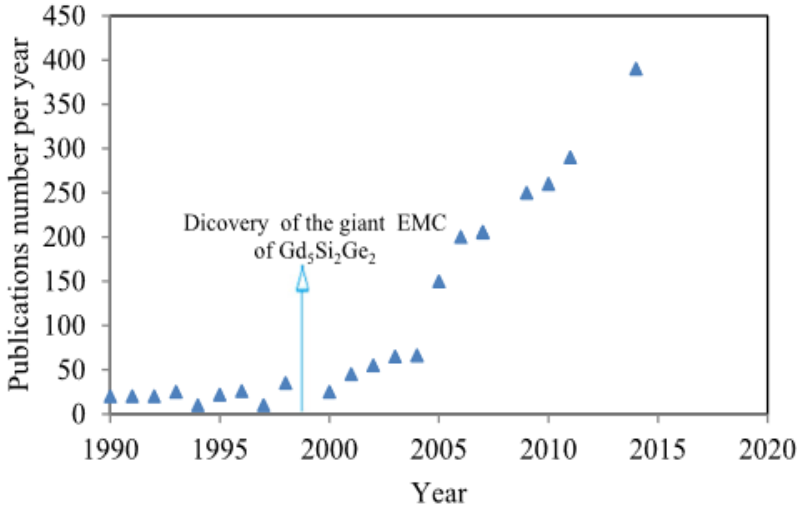

Figure 1.3 The quantity of writings that use the term "magnetocaloric" in their annual publications **(Lionte, 2015)**.

A number of searches, including one conducted in manganite materials by Phan & Yu (2007), examine the magnetocaloric effect in magnetic materials. Structured ferromagnetic perovskite manganese ($R_{1-x}M_xMnO_3$, where R = Pr, La, Nd, and M = Ca, Ba, Sr, etc.) is discussed in this paper. Because of its remarkable magnetocaloric properties and affordable production costs, researchers compared the MCE of this manganite material to those of other materials

and concluded that manganite materials are a promising option for upcoming magnetic refrigeration technologies **(Phan & Yu, 2007).**

Also, there is another study done by Kadiyala and coworkers (2018). This review examines all types of magnetic materials, including glass ceramics, ferromagnetic perovskites, spinel ferrites, and oxide-based composites. The authors believe that manganite has the potential for use in magneto refrigeration technology by a comparative examination of magnetocaloric characteristics **(Kadiyala et al., 2018)**.

1.4 Specific objectives of this work

- Clarify the magnetocaloric effect and its different types and history.
- Study the current trends in magnetocaloric materials research.
- High lighting the families of alloys and compounds that are gaining attention in the recent years.
- Discuss the novel approaches in the literature that can be used to analyze these properties that could improve the applicability of magnetocaloric materials.
- Compare between characterization methods of magnetocaloric materials.

CHAPTER TWO

THEORITICAL BACKGROUND

2.1 Introduction

Magnetocaloric effect is a phenomenon dependent on thermodynamics especially the magnetic entropy change (ΔS_M) and adiabatic temperature change (ΔT_{ad}), in this phenomenon, the (magnetic field and magnetization) are related to temperature and entropy, and the MCE can be calculated experimentally by direct and indirect methods dependent on the magnetization and/or heat capacity **(Tishin & Spichkin, 2003)**, when an magnetic field applied to a ferromagnetic material near its curie temperature the magnetic entropy decreases because the spin align parallel to the external magnetic field, then the temperature and the lattice entropy of the material increases to make up for the decline in magnetic entropy (adiabatic process), when the magnetic removed the material cool due to the increases of magnetic entropy and the spins become random **(Li, 2016)**.

Magnetic refrigerators are a significant use of the magnetocaloric effect as a replacement for gas refrigerators, although it is still under research, if new technologies are not developed and traditional cooling methods are not abandoned, it is expected that energy consumption by the year 2050will triple, due to the increase in demand for air conditioners and refrigerators in light of the population increase. Currently, air conditioners and refrigerators that rely on harmful gases consume about 2,000 TWh, which is approximately 17% of global electricity consumption **(Kitanovski, 2020)**. Additionally, the researchers predict that the magnetic

refrigerator's Carnot efficiency may approach 60%, as opposed to the gas refrigerator's 40% maximum value **(Lyubina, 2017)**.

2.2 Magnetism Classification

Magnetic materials are classified according to their bulk magnetic susceptibility (χ) as Diamagnetism, Paramagnetism, Ferromagnetism, Antiferromagnetic, and Ferrimagnetism, at room temperature as seen in figure 2.1, most elements in the periodic table exhibit Diamagnetism or Paramagnetism, which are the two most common types of magnetism **(Ghahremani, 2014).** The magnetization (M) of the material proportional to H as the following equation **(Jakubovics, 2023)**:

$M = \chi$ H…….…....(2.1)

χ isdimensionless, where H and M have the same dimensions (Am^{-1}). Also, the magnetization (M) is associated with B and H by:

$B = \mu_0(H + M)$ ……....(2.2)

By merge the two equations 2.1 & 2.2 we get:

$B = \mu_0(1 + \chi)H$ ……(2.3)

The proportionality of B and H is:

$\mu = (1 + \chi)$ …….....(2.4)

Where μ is the magnetic permeability, so by equations 2.3 & 2.4 we get:

$B = \mu_0\mu H$ ……... (2.5)

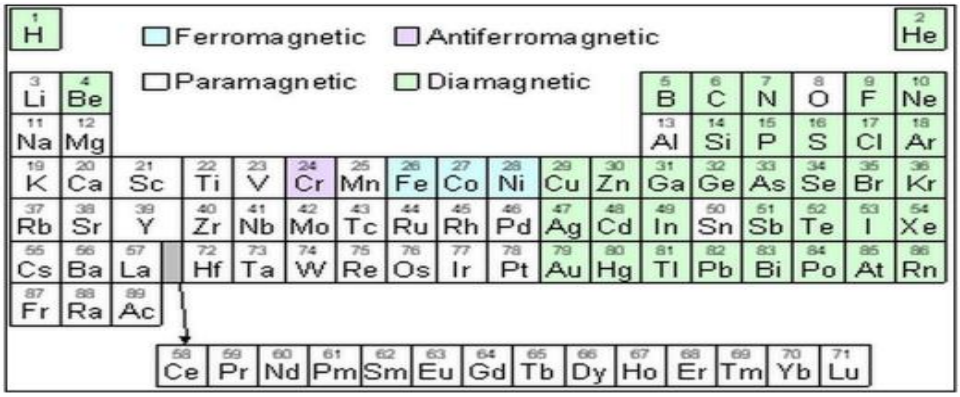

Figure 2.1 The classification of magnetic materials in the periodic table **(Ghahremani, 2014).**

2.2.1 Diamagnetism

The magnetic moment of a free atom has three principal sources: the change in the orbital moment induced by an external magnetic field, the spin of electrons, and the orbital angular momentum of electrons about the nucleus. the first effect provides diamagnetic contributions to the magnetization, whereas the second and third provide a paramagnetic contribution **(Kittel, 2005).**

Diamagnetic elements are usually called non-magnetic elements, when there is no external magnetic field, the net magnetic moment is zero as seen in figure 2. 2, under an applied field (H) the electrons produce a magnetization (M) in the opposite direction of the applied field, elements with a negative magnetic susceptibility are called diamagnetic, and this value is independent of temperature **(Ghahremani, 2014).**

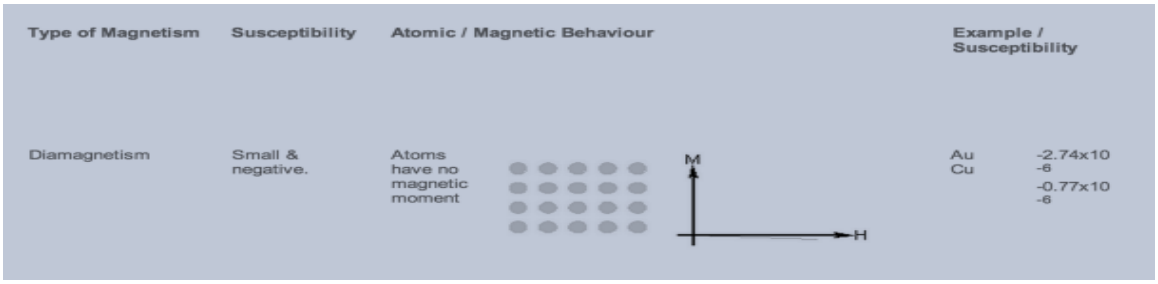

Figure2.2 The characteristics of Diamagnetic materials **(Ghahremani, 2014)**.

2.2.2 Paramagnetism

Paramagnetism theories are valid for specific types of material. Langevin model, which is suitable for materials with localized electrons (non-interacting), says that due to thermal agitation each atom has randomly magnetic moment, these materials have positive susceptibility, when there is an external magnetic field, the net magnetization is not zero as seen in figure 2.3 .

The Curie law states as the temperature increases the susceptibility will decrease, due to the increase in thermal agitation so the aligning of atomic magnetic moments will be more difficult. Curie law refers to materials in which no interaction between surrounding magnetic moments, an example of these materials is the hydrated salts of the transition metals, e.g., $CuSO_{4.5}H_2O$. But Curie-Weiss law it is refers to ferromagnetic materials due to the interaction between magnetic moments.

$\chi = \frac{C}{T}$Curie law……..(2.6)

where: C: The Curie constant, χ:The susceptibility.

$\chi = \frac{C}{T-\theta}$Curie-Weiss law……...(2.7)

Where:θ :is a Curie-Weiss constant.

There are different cases of θ when it is equal to zero, then Curie-Weiss law matches the Curie law, and the other cases θ is negative then below the transition temperature (Néel temperature, T_N) the material becomes antiferromagnetic, or θ is positive then below the transition temperature (Curie temperature, T_C) the material becomes ferromagnetic above these transitions temperatures the material become paramagnetic **(Ghahremani, 2014)**.

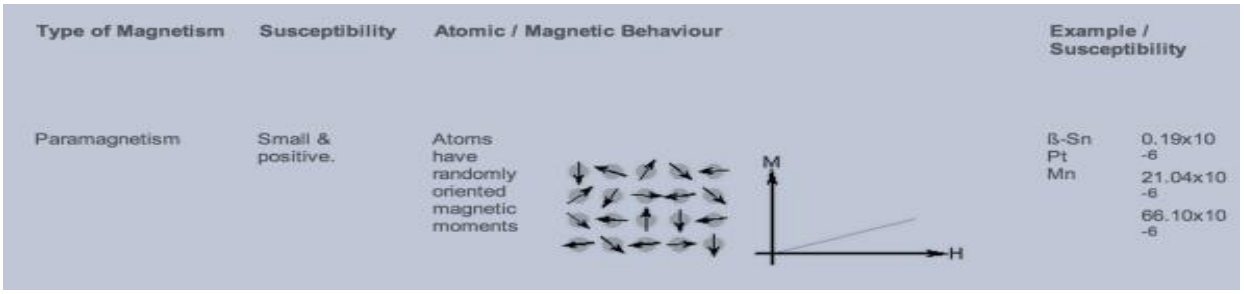

Figure 2.3 The characteristics of Paramagnetic materials **(Ghahremani, 2014)**.

2.2.3 Ferromagnetism

The Ferromagnetic material has a saturation moment which is a spontaneous moment even though the external field is zero, according the classical perspective the spontaneous moment is due to the presence of a field called molecular field this field comes from all the molecules in the sample by Weiss in 1907, and assumed that this field is proportional to the magnetization and the constant of proportional is λ, but from a quantum perspective, this field is due to the exchange interaction between neighboring moments **(Ghahremani, 2014; Kittel, 2005)**:

$B_E = \lambda M$……(2.8)

Where B_E: $molecular field$, λ: Weiss constant, M: Magnetization (magnetic moment per unit volume).

According to Weiss the ferromagnetic materials split into domains as seen in figure 2.4 (regions with magnetic moments aligned in various directions)in the demagnetization state, but in the magnetization state these domains become one domain with magnetic moments in the same direction in response to the external magnetic field as seen in Figure 2.5 **(Cullity& Graham, 2011)**.

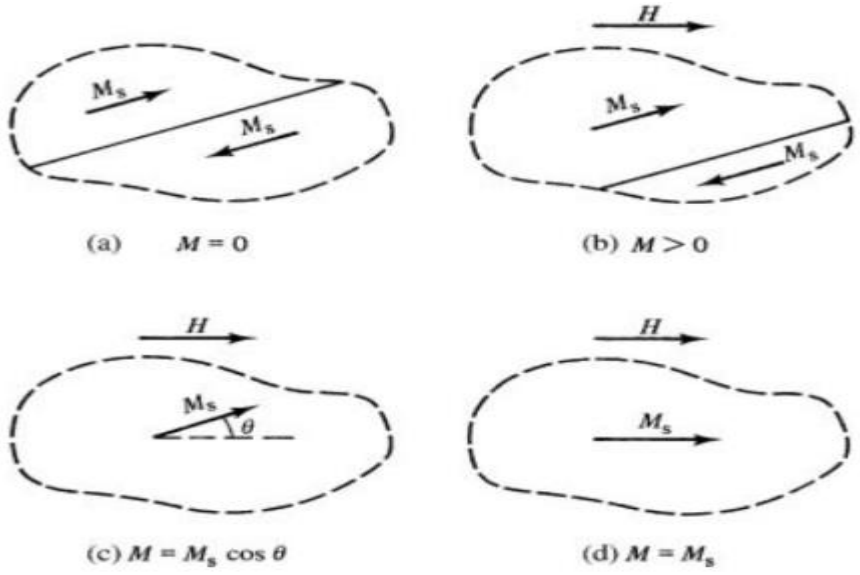

Figure 2.4 Response of ferromagnetic materials to an external magnetic field, Ms: the saturation magnetization**(Cullity& Graham, 2011)**.

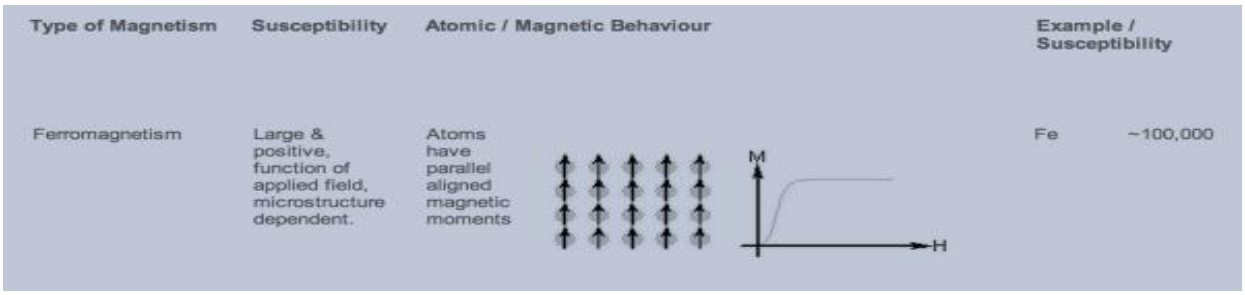

Figure 2.5 The characteristics of ferromagnetic materials **(Ghahremani, 2014)**.

2.2.4 Ferrimagnetism

Ferrimagnetism does not arise, in a single atom just in complicated structures (crystals), inside these materials, some atoms are aligned anti-parallel but others, are aligned parallel this is due to the exchange interactions inside this material as seen in figure 2.6, there are in common between these materials and the ferromagnetic materials in magnetic characterization, but the ferrimagnetism materials with less M_s. The net magnetization of Barium ferrite ($Ba_{0.6}Fe_2O_3$) which is a unit cell contains 64 ions comparatively low, due to that only ⅛ of the ions participate to the material's magnetism **(Ghahremani, 2014)**, other examples of Ferrimagnetic materials named ferrites (double oxide of iron), in 1948 Ferrimagnetism find out, and they become above transition temperature named curie temperature paramagnetic material like ferromagnetic (**Cullity& Graham, 2011)**.

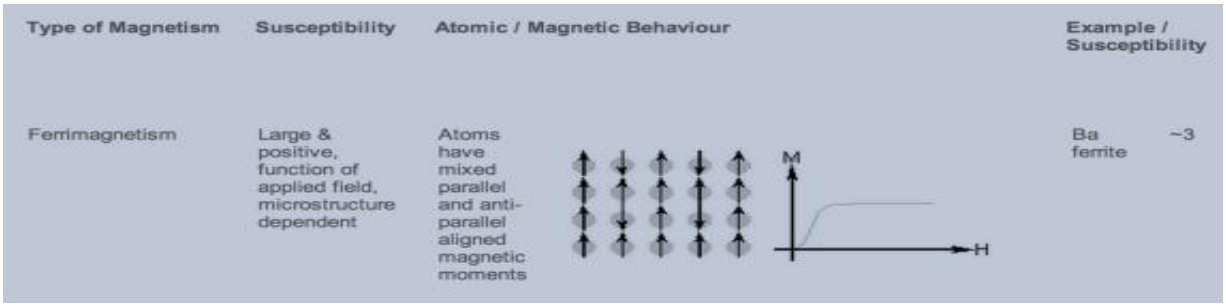

Figure 2.6 The characteristics of ferrimagnetic materials **(Ghahremani,2014)**.

2.2.5 Antiferromagnetism

Chromium is the only element in the periodic table at room temperature show exhibiting antiferromagnetic, and above a certain temperature called Néel temperature (T_N), this material becomes paramagnetic for example (Cr: $T_N = 37^0C$), when there is an applied field, the atomic

magnetic moments align anti-parallel and the applied magnetic field cancel, then the material become paramagnetic as seen in figure 2.7 **(Ghahremani,2014)**.

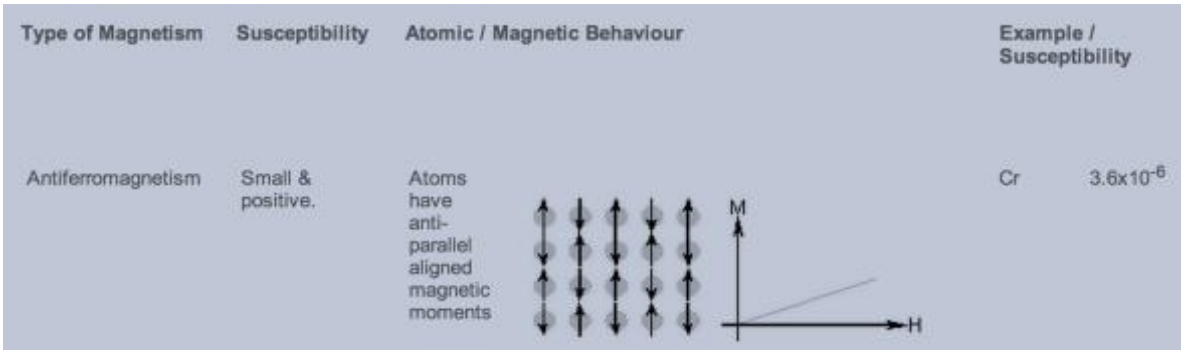

Figure 2.7 The characteristics of antiferromagnetic materials **(Ghahremani,2014)**.

2.3 Theory of the magnetocaloric effect

As mentioned above the magnetocaloric effect is a thermodynamic phenomenon that is the change in the temperature of magnetic material when exposed to an external magnetic field, the materials that show this effect are called magnetocaloric materials, these materials used in (MR) due to its efficiency. Present-day trend targets materials that have a strong MCE such as single crystalline and Polycrystalline in contrast to amorphous materials which have insufficient MCE characteristics **(Mozharivskyj, 2023)**. The strong MCE occurs at Curie temperature T_C, two types of magnetic materials could take place at the Curie temperature, that is the first and second order (FOMT) & (SOMT) materials **(Kitanovski, 2020)**.

Giauque and his pupil MacDougall demonstrated MCE effect empirically in 1933, through the use of 61 grams of hydrated gadolinium sulfate, $Gd_2(SO_4)_3 \cdot 8H_2O$, and by changing the external magnetic field Between 0.8 to 0 T, they conducted a variety of studies over 20 days, from March 19 to April 9. On the first day, the material was at a temperature of 3.4 k then reached 0.53 k, Then they began at 2k then the material cooled to 0.34 k, in the last day they reached a temperature of 0.25k from 1.5 k, and they concluded that by adiabatic demagnetization we can get low temperatures as seen in figure 2.8 **(V. K. Pecharsky & Gschneidner, 2005)**.

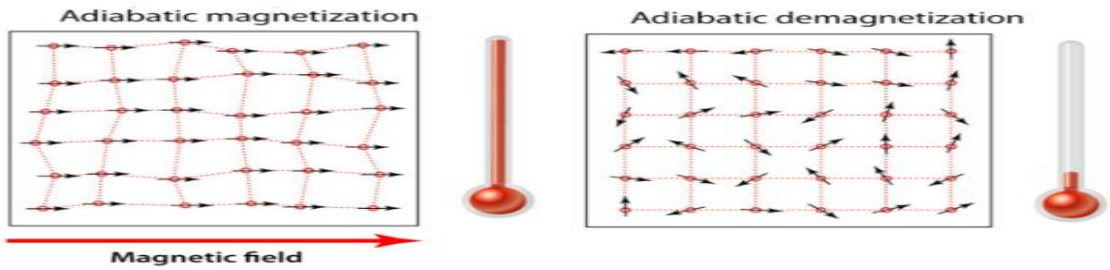

Figure 2.8 The adiabatic (magnetization, demagnetization) respectively **(Franco et al., 2012)**.

2.4 The order of magnetic phase transition

It is crucial to know the order of magnetic phase transition, by using the Inoue-Shimizu model and Landau series expansion of free energy as a function of magnetization until the sixth power, as the following equation:

$$F(M,T) = \frac{C_1(T)}{2}M^2 + \frac{C_2(T)}{4}M^4 + \frac{C_3(T)}{6}M^6 + \cdots - BM \ldots.(2.9)$$

Then according to the above equation, the magnetization near T_C becomes:

$$C_1(T)M + C_2(T)M^3 + C_3(T)M^5 = B \ldots\ldots\ldots(2.10)$$

Where by the sign of the coefficient$C_2(T)$ the order phase determines, if $C_2(\sim T_C)$ is negative (which means the slope of H/M versus M^2 curve is negative), then the phase transition is (FOMT), otherwise if the slope of H/M versus M^2 curve is positive then $C_2(\sim T_C)$ positive and the phase transition is SOMT (L.-W. Li, 2016).

2.5 Thermodynamics of MCE

The MCE is characteristic to describe the change of magnetic entropy in the isothermal process ΔS_{iso}, or it is an explanation of the fluctuations of the temperature of magnetic material in an adiabatic process ΔT_{ad} **(Basso, 2017)**. According to the temperature and magnetic field, the entropy change has three types: electronic entropy S_E is a function of temperature and describes the kinetic entropy of the electrons, lattice entropy S_L is also a function of temperature, associated with the vibration of the molecules, finally the magnetic

entropy due to the change of the order of the spin of the molecules in magnetic material as a result of an external magnetic field **(Ghahremani, 2014)** the total differential of entropy can be expressed as **(Zverev & Tishin, 2016)** :

$$ds = \left(\frac{\partial S}{\partial T}\right)_{H,P} dT + \left(\frac{\partial S}{\partial H}\right)_{T,P} dH + \left(\frac{\partial S}{\partial p}\right)_{T,H} dp \ldots.(2.11)$$

Where H: the magnetic field, p: the pressure.

The thermodynamics functions to evaluate the MCE :the Gibbs free energy G, the internal energy U and the free energy F as the following equations :

$U = U(S,V,H)$ ……..… (2.12)

Where H :the magnetic field ,V:the volume ,S:the entropy or as a function of M instead of H so the function become:

$U = U(S,V,M)$…….(2.13)

The differential form of the internal energy:

$dU = Tds - pdv - MdH$…….....(2.14)

Or

$dU = Tds - pdv - HdM$…….....(2.15)

Where T:the absolute temperature, and p:the pressure.

$F = U - TS$……..…….(2.16)

Where F is the free energy and applied in the systems with constant volume the following equation is the differential form of the free energy:

$dF = -SdT - pdV - MdH$……....(2.17)

The following equation applied in the systems at constant pressure called the Gibbs free energy G:

$G = U - TS + PV - MH$……(2.18)

The differential form of the G:

$dG = Vdp - SdT - MdH$……...……(2.19)

In the Gibbs free energy the parameters M, S and P are related to T, H, and V as the following equations:

$S(T,H,P) = -\left(\frac{\partial G}{\partial T}\right)_{H,P}$……....(2.20)

$M(T,H,P) = -\left(\frac{\partial G}{\partial H}\right)_{T,P}$……..….... (2.21)

$V(T,H,P) = \left(\frac{\partial G}{\partial P}\right)_{T,H}$……...…(2.22)

Now for the free energy:

$S(T,H,V) = -\left(\frac{\partial F}{\partial T}\right)_{H,V}$……...(2.23)

$M(T,H,V) = -\left(\frac{\partial F}{\partial T}\right)_{V,T}$……..… (2.24)

$P(T,V,H) = -\left(\frac{\partial F}{\partial T}\right)_{H,T}$…….….(2.25)

If M is used in place of H then :

$H = \left(\frac{\partial G}{\partial M}\right)_{T,P}$……... (2.26)

The following equations called Maxwell equations obtained from equations (2.20) & (2.21), (2.20) & (2.22), and (2.20) & (2.26).

$\left(\frac{\partial S}{\partial H}\right)_{T,P} = \left(\frac{\partial M}{\partial T}\right)_{H,P}$…….(2.27)

$\left(\frac{\partial S}{\partial P}\right)_{T,H} = -\left(\frac{\partial V}{\partial T}\right)_{H,P}$……..(2.28)

$\left(\frac{\partial S}{\partial M}\right)_{T,P} = -\left(\frac{\partial H}{\partial T}\right)_{M,P}$…….(2.29)

By using the following equations:

$C_X = \left(\frac{\delta Q}{dT}\right)_x$ (where $C_X$the heat capacity at constant x) & $dS = \frac{\delta Q}{T}$ ……....(2.30)

Then obtained the below equation:

$$C_X = T\left(\frac{\partial S}{\partial T}\right)_X \text{.....(2.31)}$$

And, by using the following equation:

$$\alpha_T(T,H,P) = -\frac{1}{V}\left(\frac{\partial S}{\partial P}\right)_{T,H} \text{..... (2.32)}$$

Where α_T the bulk thermal expansion coefficient.

Then by using equations (2.27), (2.31), and (2.32), equation (2.11) under the adiabatic process becomes:

$$\frac{C_{H,P}}{T}dT + \left(\frac{\partial M}{\partial T}\right)_{H,P} dH - \alpha_T V dp = 0 \text{.....(2.33)}$$

Where $C_{H,P}$is the heat capacity at constant pressure and magnetic field.

In magnetocaloric experiments when $dp = 0$ (adiabatic–isobaric experiment) then the following equation is derived:

$$\Delta T_{ad}(T)_{\Delta H,P} = -\int_{H_1}^{H_2}\left(\frac{T}{C(T,H)} \times \frac{\partial M(T,H)}{\partial T}\right)_{H,P} dH \text{.... (2.34)}$$

The following equation obtained by Maxwell relations:

$$\Delta s_M(T)_{\Delta H,P} = \int_{H_1}^{H_2}\left(\frac{\partial M(T,H)}{\partial T}\right)_{H,P} dH \text{..... (2.35)}$$

Where $\Delta s_M$is the magnetic entropy change.

Equations (2.34) & (2.35) can't be solved by analytical solution because the heat capacity and magnetization are functions of magnetic field and temperature that vary by material and are typically unknown. Equation 2.35 is frequently solved by numerical solution, unlike equation 2.34 which is rarely integrated as a result of the heat capacity which depends on temperature and magnetic field which isn't known with the necessary details, also both equations do not succeed in finding MCE in (FOMT) because the first derivative does not exist **(V. Pecharsky et al., 2001; Tishin & Spichkin, 2003).**

In the following topics, a summary of the experimental method of determination of MCE will be discussed (direct and indirect measurements).

2.6 Inverse MCE

When the magnetic material is exposed to an external magnetic field the MCE is divided into two distinct effects the inverse and traditional MCE **(Tran et al., 2022)**, as mentioned above the MCE depends on magnetic entropy change (ΔS_M) and adiabatic temperature change (ΔT_{ad}), in the traditional effect the entropy decreases with magnetization at the isothermal process, but in the inverse case the entropy increases at the isothermal processes, the other difference between them is the temperature at the adiabatic processes, where in the direct effect the temperature increase but in the inverse decrease **(Kamantsev et al., 2023)**. In another sense, the magnetic material at adiabatic conditions, in the direct effect when exposed to an external field warms up, but in the inverse effect, the material cools down with magnetization **(Ranke et al., 2009)**.

Examples of magnetic systems that show inverse effect are antiferromagnetic (AFM) systems with small changes in magnetic field and the change in ΔS_M is relatively small, also in Heusler alloys like in NiMnSn **(Zheng et al., 2017)**. It is used when necessary to cool the magnetic system as fast as possible **(Kamantsev et al., 2023)**. The inverse and traditional MCE are noticed at the transition temperatures (Néel temperature T_N, Curie temperature T_C) **(Aliev et al., 2011)**.

2.7 Determination of MCE

There are two methods for measuring the magnetocaloric effect, the first one is the direct measurement, which involves measuring the difference in temperature in an adiabatic process when the material is exposed to a change in a magnetic field, the second method for measuring is the indirect measurement of magnetic entropy change and the magnetocaloric effect in the frame of Magnetization in addition to heat capacity **(Tishin & Spichkin, 2003).**

2.7.1 Direct determination of MCE

In this technique, the initial and final temperatures are measured by changing the external magnetic field so the change in the adiabatic temperature is measured by the following equation:

$\Delta T_{ad}(T_0, H_f - H_i) = T_f - T_i$ …… (2.36)

Where: $H_0 =$ the initial value of the external magnetic field.

$H_f =$ the final value of the external magnetic field.

$T_i =$ the initial tempresure of the sample.

$T_f =$ the final tempresure of the sample.

Direct measurements depend on whether the temperature sensor is directly attached to the sample or not **(Casanova iFernàndez, 2004)**, they may be by changing the pulsed magnetic field and fixing the sample, or by going the sample within and outside of a constant magnetic field **(Tishin & Spichkin, 2003)**. Weiss (1921) first provides the direct technique, However, this technique has some significant drawbacks, such as the temperature sensitivity is small so the study of the small samples excludes (films, microwires, and ribbons), and the uncertainty is extremely high(7-15 %) **(Aliev et al., 2011)**. The accuracy of this technique in the range of 5-10%, is affected by the surroundings of the field, errors in the measurement of temperature (thermometry), and sample thermal insulation quality **(Casanova iFernàndez, 2004)**.

2.7.2 Indirect determination of MCE

In this method the MCE is measured by using both the heat capacity and magnetization, magnetization may be used to measure only ΔS_M (T,ΔH), whereas ΔT_{ad} (T,ΔH),ΔS_M (T,ΔH), both can be measured by the heat capacity measurements, in comparison with the direct measurements, which only just provide the ΔT_{ad} (T,ΔH)**(Casanova iFernàndez, 2004)**.

Special tools are needed to measure heat capacity as a relationship of temperature at different measurements of the magnetic field as well as for direct measurements, so measurement using magnetization as a function of temperature and magnetic field is the most widely used method, using magnetization curves ΔS_M (T,ΔH) can be calculated by numerical integration of Eq.(2.35) **(Casanova iFernàndez, 2004; Jeppesen et al., 2008)**.The mistakes in

determining ΔS_M (T,ΔH) value by this method in the range 3-10 % as a result of using (ΔT,ΔM, and ΔH) instead of (dT, dM, and dH) in Eq.(2.35), also the precision in the ΔS_M (T,ΔH) relies on the precision of the Magnetic moment measurements **(Casanova iFernàndez, 2004)**.

Now, as mentioned previously another method to determine ΔS_M (T,ΔH) is the heat capacity at constant pressure and magnetic field as the following equations :

$$\Delta S_M(T) = S(T)_{H_F} - S(T)_{H_I} \ldots\ldots\ldots\ldots\ldots\ldots\ldots\ldots\ldots\ldots (2.37)$$

$$S(T)_{H_{I,F}} = \int_0^T \frac{C(T)_{H_{I,F}}}{T} dT + S_{0,H_{I,F}} \ldots\ldots\ldots\ldots\ldots\ldots\ldots\ldots (2.38)$$

Where I: the initial state, F: is the final state, and S_0: is zero temperature entropies **(Jeppesen et al., 2008)**. Also, ΔT_{ad}(T,ΔH) can be determined by $S(T)_{H_{I,F}}$, the precision in the ΔS_M (T,ΔH) and ΔT_{ad}(T,ΔH) relies on the precision of the $C(T)_{P,H}$ **(Casanova iFernàndez, 2004)**.

2.8 Magnetic cooling efficiency

To calculate the magnetic cooling effectiveness of a magnetocaloric material, just evaluate ΔT_{ad} (maximum adiabatic temperature change) or ΔS_M (maximum magnetic entropy change), with its full-width at half maximum $\delta T_{FWHM} = (T_2 - T_1)$ as seen in figure 2.9 so the calculation of the relative cooling power (RCP) is **(Phan & Yu, 2007)**:

$$RCP(S) = -\Delta S_M(T, H) \times \delta T_{FWHM} \ldots\ldots\ldots (2.39)$$ (Relative cooling power based on ΔS_M).

$$RCP(T) = \Delta T_{ad}(T, H) \times \delta T_{FWHM} \ldots\ldots\ldots\ldots (2.40)$$ (Relative cooling power based on ΔT_{ad}).

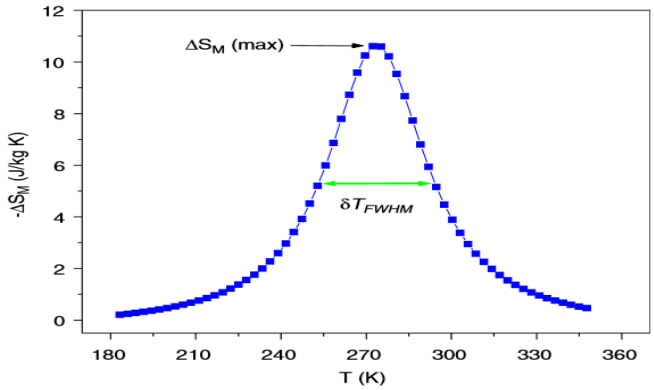

Figure 2.9 RCP for a $La_{0.7}Ca_{0.25}Sr_{0.05}MnO_3$ single crystal **(Phan & Yu, 2007)**.

CHAPTER THREE

EXPERIMENTAL PROCEDURES

(Instruments and Techniques)

3.1 Introduction

This chapter will examine some of the methods used by researchers to analyze crystallization structure and the different synthesis techniques used to prepare the single and polycrystalline crystals.

3.2 Synthesis techniques

Polycrystalline materials are commonly melted using the arc melting process **(Benka, 2021)**.When working with single crystals, many techniques are used, such as the Bridgman processes **(Radelytskyi et al., 2017)**. The optimum approach depends on the specific materials being used.

3.2.1 The arc melting techniques

The "arc melting" techniques came to light in the late 1960s, according to figure 3.1, a typical arc melting devices is made up of several parts, like two electrodes: a copper bottom electrode called a crucible that holds the reactants and is cooled by water, and a top-mounted, detachable tungsten electrode. It is feasible to remove the atmosphere from the chamber and replace it with argon using a vacuum pumping system. Furthermore, there is a melting chamber where the elements melt.

The initial powders are intensively mixed together using an crucible and a agate mortar. After that, the mixture is compressed to create pellets. In order to prevent the powder from being ground up by the electrical arc during the synthesis, it is imperative that the powder mix be compressed. Within the reaction chamber, the pellets are set up on a copper electrode that is cooled by water. A voltage is supplied between the two electrodes after the argon is pumped into and filled into the reaction chamber. Up until the electrical arc forms, the higher tungsten electrode is manually pushed in close proximity to the sample. The entire sample melts quickly as a result of the arc. The resulting liquid ball cools quickly because of the contact with the copper disk causes the produced liquid ball to cool down quickly. There is still some un melted powder in the bottom portion of the sample that is in contact with the copper disk at this time. To guarantee that the sample has completely melted, the entire procedure is performed three times, each time with the ball returned. To prevent any contamination of the subsequent samples, the copper crucible and the entire chamber are cleaned after a sample is synthesized **(Gerin, 2022)**.

This technique can achieve temperatures above 3500 °C **(Benka, 2021)**. Examples of materials produced by arc melting are HEAs **(Al-Shataif et al., 2019)** and the $La(Fe,Si)_{13}$ **(Vinod et al., 2024).**

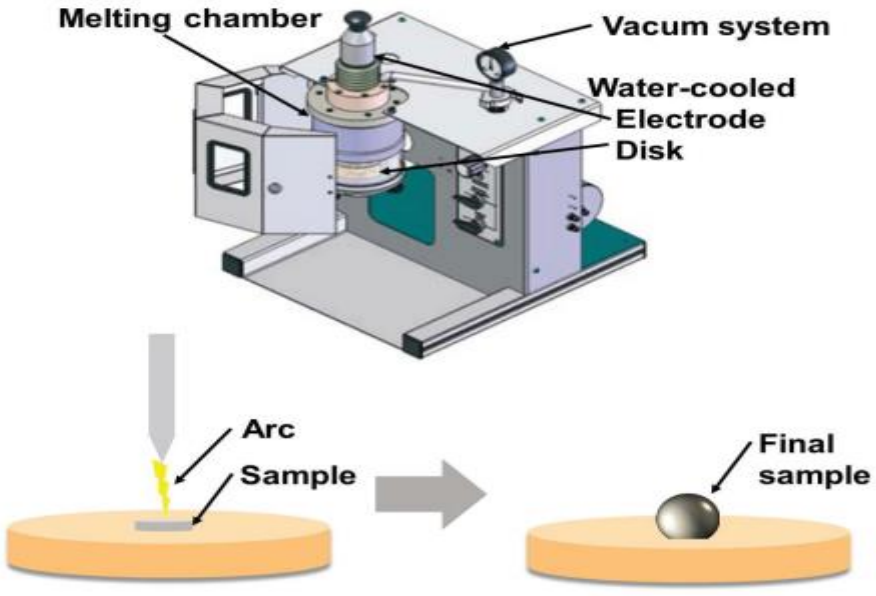

Figure 3.1The arc melting technique's apparatus **(Gerin, 2022)**.

3.2.2 Single crystal growth: The Bridgman method

The Bridgman Method is divided into two zones, as seen in figure 3.2, the cold zone and the hot zone, with temperatures exceeding the material's melting point **(Venkataraman, 2020).** The end of the container where a crystal begins to grow may be extended, and a seed crystal can be positioned at that end to aid in the growth of the crystal with temperature below the melting point **(Mozharivskyj, 2023; YU & Cardona, 2010)**. The crucible can be positioned vertically or horizontally **(YU & Cardona, 2010).** An example of material prepared by Bridgman's method is Ni_2MnGa **(Radelytskyi et al., 2017)**.

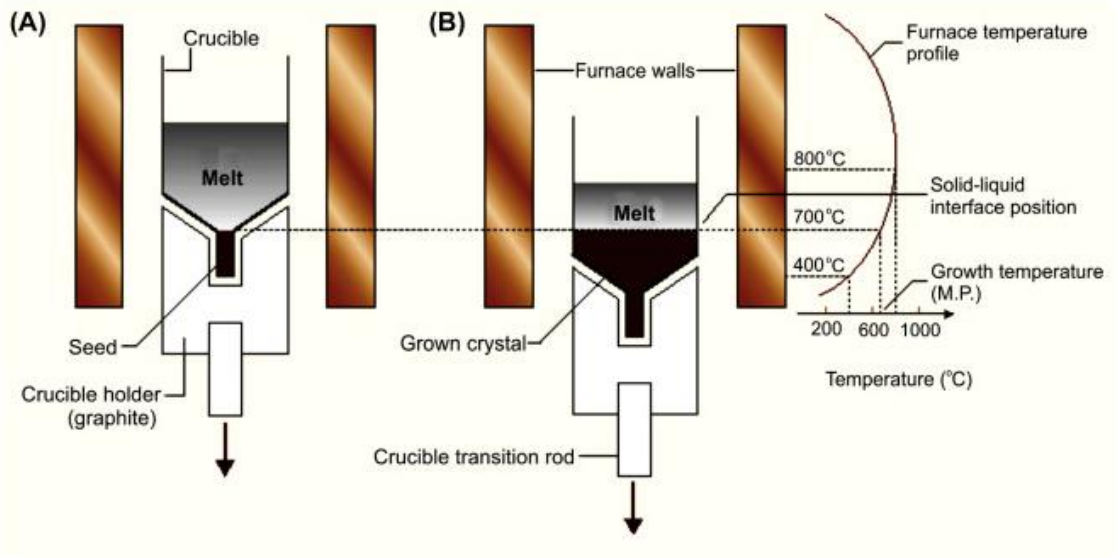

Figure 3.2 Schematic illustration of a vertical Bridgman crystal growth process in a single-zone furnace: (A) at the start of the experiment in the hot zone, and (B) as the partially produced crystal moves through the cold zone **(Venkataraman, 2020)**.

3.3 Crystallographic characterization techniques

3.3.1 Basics of scattering and diffraction techniques

Scattering occurs when the radiation is emitted in different directions as a result of collisions with the sample or the interference of the electromagnetic wave **(Wade & Drake, 2019)**. Scattering techniques are beneficial methods for providing information about the properties of crystal structure; in other words, these techniques shed light on the microscopic properties of

the crystal structure. If suitable radiation is selected, then this technique is non-destructive **(Al-Namourah, 2019)**. This technique operates better when the size of the sample that scattered the electromagnetic wave is the same as the wavelength of the electromagnetic wave **(Cipelletti et al., 2016)**. An example of elastic scattering is X-ray diffraction, which is a harmless method **(Whittig & Allardice, 1986)**.

X-ray diffraction is used to provide information about the distance among the atomic planes, the arrangement of the atoms in the unit cell, and their positions. When the X-rays scatter in different directions, the waves interfere as a distractive or constructive interference. According to the Figure 3.3, there is a strong relationship between the internal arrangement of the atoms (periodicity) and the diffraction. The crystalline material demonstrates many maximums. X-ray diffraction peaks: in the contract, there is only one peak in the amorphous materials as a result of the disordered arrangement of the atoms. The intensity of the diffraction peaks gives information related to the atomic (position and number), but the data of the shape and the size is provided by the positions of the diffraction peaks **(Ali et al., 2022)**.

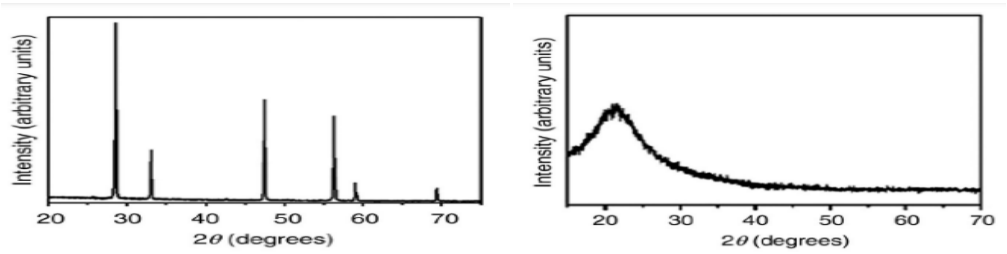

Figure 3.3 XRD graphs at different diffraction angles of (left) crystalline material and (right) amorphous materials **(Lamas et al., 2017)**.

According to Robotti (2013), X-ray diffraction by using crystal was discovered in 1912 by Laue **(Robotti, 2013)**, then Bragg used XRD to determine the interspaces and distance between layers of atoms (equally spaced parallel planes) in crystals (d). In addition to knowing and understanding of crystal diffraction, when X-ray hits the planes by θ, the incident beam is scattered also by the same θ. According to Bragg condition, the interference is constructive when the path difference equals an integer number of ג (the wavelength of the incident beam). The deriving of this condition is as follows **(Ali et al., 2022)**:

According to the small right triangles in figure 3.4:

$sin\theta = \frac{AB}{d},\ sin\theta = \frac{BC}{d}$…….(3.1)

Then according to Bragg's condition for constructive interference:

$AB + BC = n\lambda$…….(3.2)

Now, according to the equation 3.1:

$dsin\theta + dsin\theta = n\lambda$……..…….(3.3)

Then:

$2d \sin\theta = n\lambda$…….……..(3.4)

Where n: the order of diffraction (reflection).

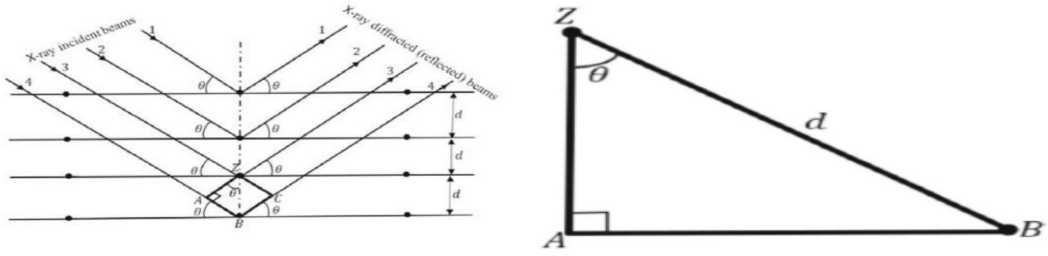

Figure 3.4 XRD pattern (left) and right triangle to derive the Bragg condition (right) **(Sivia, 2011)**.

As shown in Table 3.1 below, there are four different kinds of diffraction techniques based on the crystalline sample types (polycrystalline powder and single crystal), in addition to the radiation kinds (polychromatic and monochromatic**) (Sochi, 2010)**.

Table 3.1 The different types of diffraction techniques (Sochi, 2010).

	Monochromomatic Radiation	Polychromatic Radiation
Single Crystal	Bragg	Laue
powder	Angle Dispersive	Energy Dispersive

3.3.2 X-ray powder diffraction

X-ray powder diffraction is an old and versatile technique that uses X-ray radiation to determine the atomic structure of polycrystalline powder material, which is a huge number of randomly ordered single crystals **(Von Dreele & Toby, 2012).** Much information can be obtained from the analysis of the diffraction pattern of XRPD, such as the different quantitative states or phases of the solid material, lattice constants, and crystalline sizes **(Clearfield & Bhuvanesh, 2008; Iwashita, 2016).** Using Debye Scherrer's equation, the crystalline size can be ascertained from X-ray diffraction as follows **(Fatimah et al., 2021)**:

$$D = \frac{K.\lambda}{\beta \cos\theta} \text{.....(3.5)}$$

Where D is the crystalline size,λ is the wavelength of the X-rays used, K is the Scherrer constant,θ is the peak position, and β is the Full Width at Half Maximum ($FWHM$).

When the powder sample is exposed to X-ray radiation, all diffraction peaks from each lattice plane will be observed. These peaks begin at the center of the crystal, then extend outward with certain scattering angles and form cones, which are known as Debye-Scherrer cones. These cones produce concentric rings when focused on a flat surface perpendicular to the incident beam, called Debye-Scherrer rings, as seen in the figure 3.5. The diffraction patterns can be obtained by rotationally averaging the Debye rings, and the intensity (I) of each ring as a function of the scattering angles (2θ) can be calculated by integrating the whole ring **(Sochi, 2010)**.In the next section, there is information about a device used to record diffraction patterns.

3.3.2.1 Powder Diffractometers

Powder diffractometers are equipment used to record the diffraction patterns produced by X-rays as seen in figure 3.5 **(Ladd & Palmer, 2013)**. This device consists of a monochromator or filter, an X-ray source, the sample stage, a detector, and a collimator. The X-ray source gets polychromatic radiation; to obtain monochromatic radiation, there are two methods. The first is a monochromator, where a single crystal is used to get monochromatic radiation by

diffraction and Bragg's law. The second method is filters, where a thin sheet is used that absorbs all unwanted wavelengths **(Al-Namourah, 2019)**.

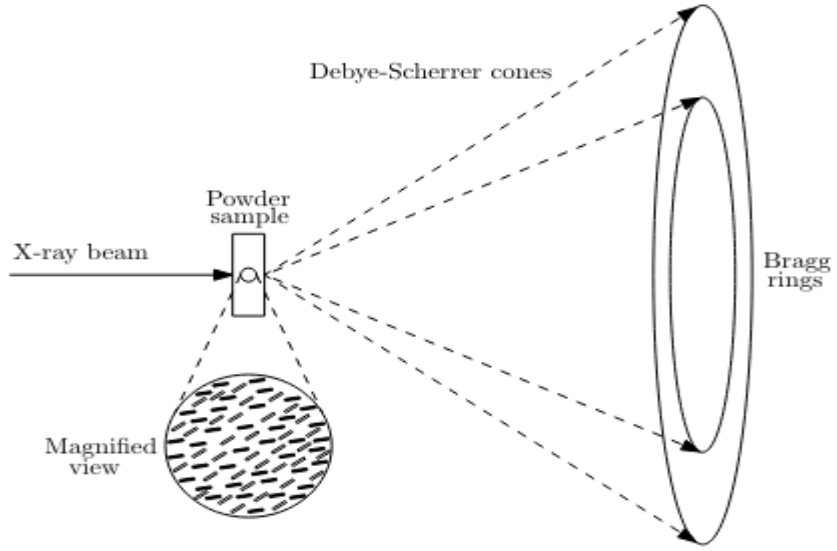

Figure 3.5 Bragg rings and Debye-Scherrer cones **(Sochi, 2010)**.

3.3.3 Laue diffraction

Laue diffraction is the earliest technique of the X-ray diffraction techniques. This technique is used to determine the orientation and symmetry of a single crystal. Polychromatic white radiation is used in the Laue method; each diffracted radiation has a characteristic wavelength. The diffraction pattern is recorded by a device called an X-ray camera, which holds a sample and photographic film **(Clearfield & Bhuvanesh, 2008; Lee, 2016)**. A Laue diffraction pattern is produced when polychromatic X-rays strike a crystal that has been diffracted to the film by the crystal planes. In 1912, Knipping, Laue, and Friedrich created the first Laue diffraction pattern. According to Bragg's law ($2d \sin\theta = n\lambda$) a single diffraction spot may arise from reflections corresponding to different interplanar spacing (d) (e.g., d, d/2, d/3, etc.) and different wavelengths (λ)(e.g., λ, $\lambda/2$, $\lambda/3$, etc.) **(Drenth, 1994)**.

The Laue technique has two various configurations: the first is the back reflection method, and the second is the transmission Laue method, which depends on the order of the crystal, X-ray tube, and recording film **(Lee, 2016)**. The position of the spot on the film depends on

the wavelength of the diffracted X-ray radiation but does not depend on the distance between the planes **(Cullity, 1978)**.

3.4 Crystal structure analysis

3.4.1 Qualitative phase analysis

The qualitative analysis used to determine crystal phase identification, peak position and intensity related to unique crystal structure, by using databases such as ICDD (International Centre for Diffraction Data), COD (Crystallography Open Database). Comparing the unknown pattern to a database of single-phase reference patterns is the fundamental process of phase identification **(Sutrisno et al., 2018)**.In other words, crystalline phases are present in the samples can be determined by using X-ray qualitative phase analysis. Every polycrystalline phase exhibits a unique X-ray pattern with distinct diffraction line positions and intensities. In qualitative X-ray analysis, information from the ICDD database is compared with experimental diffraction data, including relative intensities, d_{hkl} interplanar distances, and 2θ diffraction angles . The Bragg Equation was used to calculate the values of the d_{hkl} interplanar distances **(Jendrzejewska et al., 2021)**.It is typical to observe a diffraction line shift of less than 0.2 when examining a polycrystalline material. It has to do with a polycrystalline sample's randomly arranged grains. Conversely, changes greater than 0.2◦ at a specific diffraction angle of 2θ suggest the presence of an alternative crystal structure **(Jendrzejewska, 2020)**.

3.4.2 Quantitative phase analysis

Quantitative diffraction data analysis involves figuring out how much of each phase is present in multi-phase samples. Because the concentration of a phase or phases in a mixture determines the strength of their diffraction pattern, quantification is possible **(Sutrisno et al., 2018)**.

3.4.2.1 Le Bail method

The structure of the crystal is calculated by different techniques, with each technique giving slightly different results. To adjust these results, a Le Bail fitting is used to determine the best technique or to increase their precision. The Le Bail method is used to minimize the difference between calculated patterns (from software based on the structure parameters) and measured patterns by adjusting the crystal parameters, also an iterative method.

The Le Bail method depends on the decomposition of the measured patterns into individual peaks as seen in figure 3.6 **(Mařík & Šimeček, 2015)**, then the calculated pattern obtained by using the primary values of unit cell parameters compared to measured patterns, then the difference between the two patterns minimized by refining the background parameters, unit cell parameters, zero shift parameter, and profile function. After that new diffraction profile was calculated, the first step was repeated until the two patterns agreed. The following numerical factor which is called the profile R-factor (Rp) used to assess the agreement between the calculated and measured diffraction profile:

$$R_p = \frac{\Sigma_j |y_{obs,j} - y_{cal,j}|}{\Sigma_j y_{obs,j}} \quad \text{..... (3.6)}$$

Where:

$y_{obs,j}$ and $y_{cal,j}$ are the observed and calculated intensity at a single point in the diffraction pattern, respectively **(Abboushi, 2021)**.

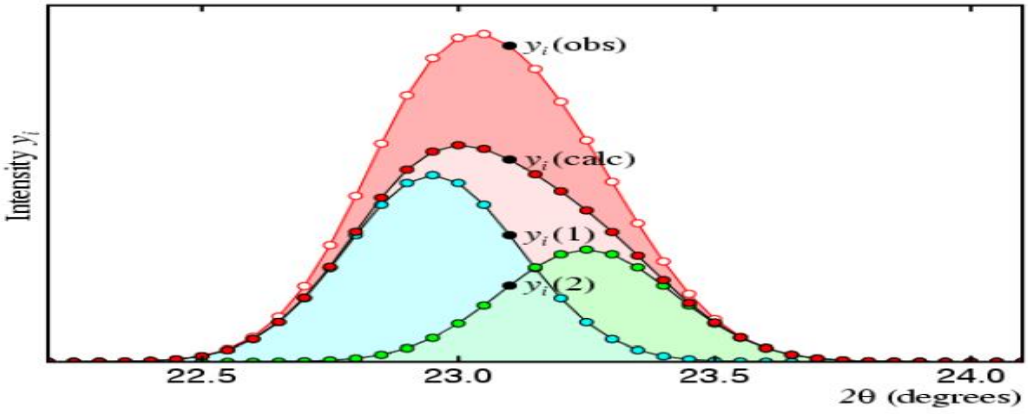

Figure 3.6 Decomposition pattern **(Mařík&Šimeček, 2015)**.

3.5 Magnetization measurement

3.5.1 Heat capacity: Physical Property Measurement System (PPMS) Dynacool

The PPMS is an instrument that measures the sample's thermodynamic and magnetic characteristics, such as heat capacity **(Nazzal, 2023)**. The average heat capacity at constant pressure is$C_p = {dQ}/{\Delta T}$, where$\Delta T = T_2 - T_1$ is the change in the temperature of the sample, and dQ is the thermal energy removed from or added to the sample, figure 3.7 schematically depicts the PPMS heat-capacity puck, which has thermal connections to both the sample platform and the sample. A thin layer of Apiezon grease is used to mount the sample on the puck's platform for heat capacity measurements. Thin platinum wires hold the platform in place in the center of the puck frame. These wires also serve as electrical connections for the heater and thermometer, which are mounted to the platform's bottom. Thermal conduction between the heater/thermometer and the thermal bath improves the thermal equilibrium between the sample and the platform. In order to thermally isolate the platform, the measurements are carried out in a high vacuum environment (the thermal conductance between the sample platform and thermal bath is only given via the wires). Silver paste is used to secure the sample in magnetic field measurements so that there is adequate thermal contact between the sample and the platform and to keep the sample from coming loose **(Maraytta, 2021)**.For the heat-capacity measurement, a heat pulse method is apply, the heater is used to apply a heat pulse to the sample platform in order to test its heat capacity. The thermometer is then used to determine the platform's temperature response. The sample heat capacity must be measured in two phases. Prior to mounting the sample, the so-called addenda measurement—which involves only the grease/silver paste and the platform—must be completed in order to account for the extra heat capacity that the grease (silver paste) produces. This measurement's result is regarded as background. The sample is then put on the puck, and the combined heat capacity of the sample and grease is calculated. The sample heat capacity can be calculated by deducting the addenda from the measurement results obtained using the sample by $C_s = C_{tot} - C_P$, where C_P the heat capacity of the platform plus the silver paste, C_{tot} the sample heat capacity plus the addenda, and C_s the heat capacity of the sample **(Ghorbani-Zavareh, 2016; Maraytta, 2021).**

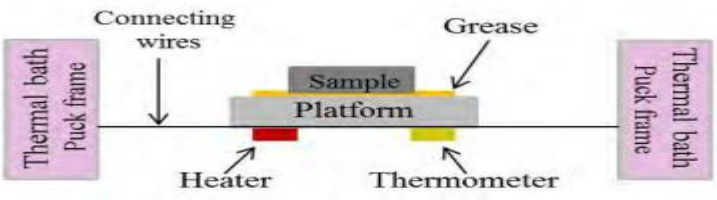

Figure 3.7 Schematically depicts the PPMS heat-capacity puck with thermal connections to sample platform and the sample **(Design, 2010)**.

3.5.2 Direct adiabatic temperature change in Pulsed Magnetic fields

The following set-up of the pulsed field experiment, as seen in figure 3.8, was used to find the adiabatic temperature change, which contains a magnet, cryostat, electronic connections, thermocouple, and sample holder; the figure also consists of images of the sample holder's two sides as well as the brass cylinder, which serves as the local heater, which is a part of the sample holder. In order to achieve adiabaticity, the sample space inside the shield was evacuated**(Ghorbani-Zavareh, 2016)**.The magnetic-field pulse's field strength was measured using a tiny pick-up coil that was placed close to the sample. The magnetic field can be calculated by integrating the induced voltage in the pick-up coil over time **(Gottschall, 2016)**.

The temperature change of the sample due to the pulsed magnetic field measured by using (Constantan – Copper) thermocouple, to prevent any open loops, the copper and constantan wires were tightly wound together. Next, one thermocouple leg—referred to as the sample junction—was squeezed between the two samples, and the other—referred to as the reference junction—was fixed on the other side of the holder to measure the sample holder's internal temperature (referred to as the reference temperature) and identify any effects the field may have had on the thermocouple voltage. The thermocouple's schematic is shown in figure 3.9 **(Maraytta, 2021)**.

To calibrate the thermocouple, temperature dependence of voltage V(T) and voltage dependence of temperature T(V) are expressed in polynomial form as seen in figure 3.10. Thus, an initial voltage V_i is produced by the initial temperature T_i. the final temperature T_f

obtained by using the T(V) function from $V_{f;}$ this can be done by increasing the initial voltage by the measured voltage change ΔV. then the change in the adiabatic temperature can be computed as $\Delta T_{ad} = T_f - T_i$. The Matlab program is used to convert mV to K **(Ghorbani-Zavareh, 2016)**.

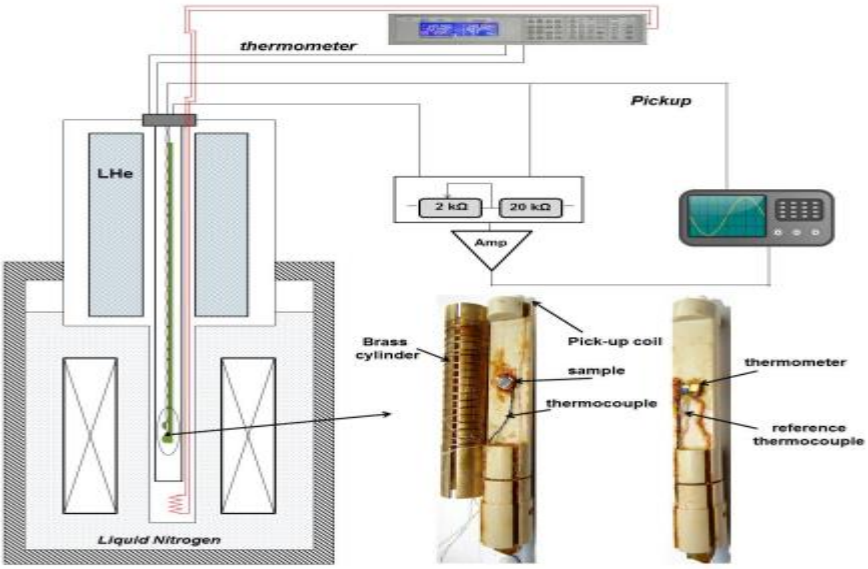

Figure 3.8 The experimental set-up for adiabatic temperature measurements in pulsed magnetic fields **(Ghorbani-Zavareh, 2016).**

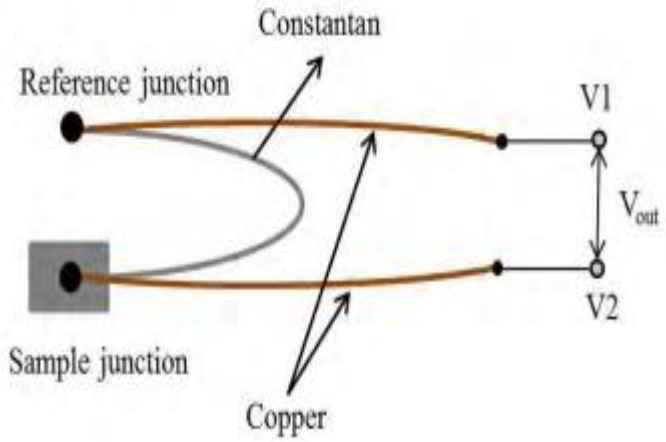

Figure 3.9 The schematic of the Constantan-Copper thermocouple **(Maraytta, 2021)**.

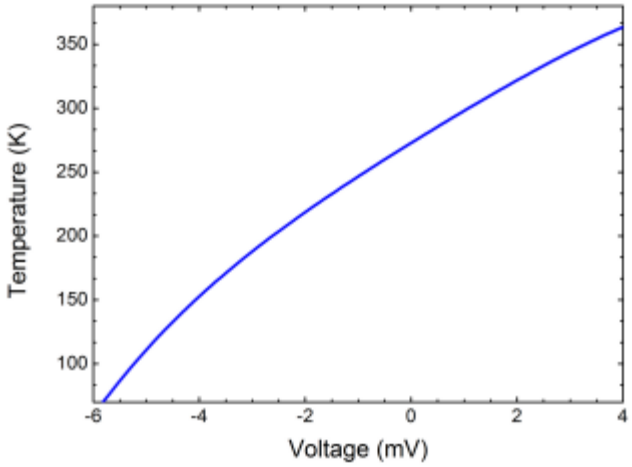

Figure 3.10 The calibration plot for (Constantan – Copper) thermocouple (T-type) **(Ghorbani-Zavareh, 2016)**.

3.5.3 Vibrating Sample Magnetometer (VSM)

The DC magnetization measurement was performed by using the Physical Property Measurement System (PPMS) DynaCool with the vibrating sample magnetometer (VSM) option. A schematic of the VSM is provided below in figure 3.11. The magnetic moment of the magnetic materials measurement is done by two protocols, the isothermal and the isofield measurement. So the magnetization measurement includes both the temperature-dependent magnetization M(T) and the magnetic field-dependent magnetization M(H) **(Nazzal, 2023)**.

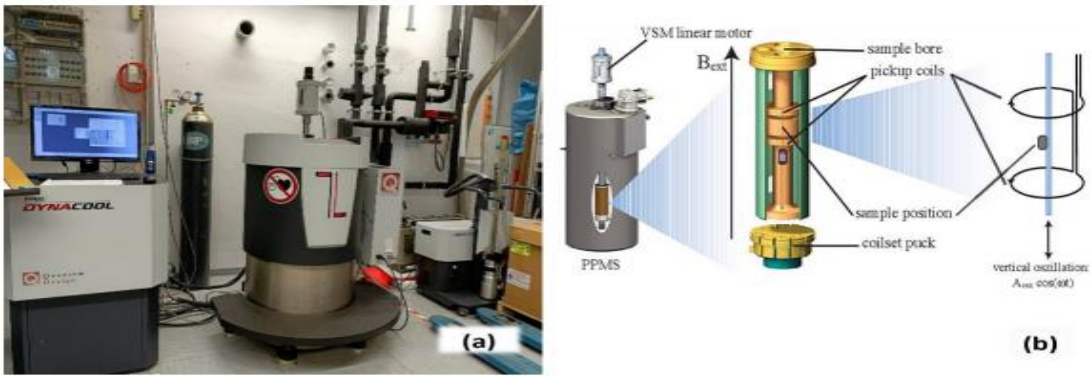

Figure 3.11 (a) PPMS DynaCool at JCNS-2 and (b) Schematic of the VSM option **(Schmid, 2008)**.

An electromagnet or superconducting solenoid to create a vertical field and a linear transport motor to vibrate the sample make up the majority of the VSM. Additionally, the system has an amplifier to enhance vibrations, pick up coils that are in close proximity to the vibrating sample, detect induced voltage, and run the motor and measure voltage through electrical devices. Furthermore, the device may be automatically controlled with the help of specialized software **(Buschow & de Boer, 2003; Nazzal, 2023)**.

The magnetic flux changes in close proximity of the sample as it vibrates along the field axis at the pick-up coils' center. Faraday's law of induction states that the change in flux induces the voltage in the pick-up coils. The following equation shows that the time-dependent induced voltage is proportional to the frequency of oscillation, the magnetic moment of the sample, and the time derivative of the magnetic flux through the coils.

$$V_{coil} = \frac{d\Phi}{dt}$$

$$= \left(\frac{d\Phi}{dz}\right)\left(\frac{dz}{dt}\right) \text{.....(3.7)}$$

Where, Φ is the magnetic flux enclosed by the pickup coil, z is the vertical position of the sample with respect to the coil, and t is time. For a sinusoidally oscillating sample position, the voltage is based on the following equation:

$V_{coil} = 2\pi fCmAsin(2\pi ft)$..... (3.8)

Where, C is a coupling constant, m is the DC magnetic moment of the sample A is the amplitude of oscillation, and f is the frequency of oscillation **(Design, 2011; Nazzal, 2023)**.

3.6 Neutron Scattering Techniques

Materials research widely employs neutron scattering techniques. One potential use for these techniques is the measurement of atomic relative mobilities and locations in solid or liquid bulk materials. The measuring of a neutron dispersed beam's intensity following the beam's passage through a sample is the fundamental process of neutron scattering **(Río-López et al., 2021)**. Neutrons can enter materials deeply and interact with matter extremely weakly because they are uncharged particles. Since there is no Coulomb barrier to cross when there is zero net charge, neutrons are assumed to ignore the charged electronic cloud and engage with

the atomic nucleus directly **(Biniskos, 2018)**. as well as the truth that neutrons interact with atoms via nuclear force rather than electrical forces, and because nuclear forces have a relatively small range, neutrons can pass through most materials at great lengths without being scattered or absorbed. Neutrons can distinguish between isotopes and neighboring elements in the periodic table by means of their interactions with atomic nuclei; this gives them an advantage over other methods like electron or X-ray diffraction **(Río-López et al., 2021)**. Despite having no net charge, neutrons have a magnetic moment because of the gluons and quarks that make up their internal structure. Due to the interaction of the neutron's magnetic moment with the unpaired electron spins of magnetic atoms, this characteristic allows the neutrons to study a material's magnetic properties, such as the magnetic structure of the sample **(Biniskos, 2018;Río-López et al., 2021)**. There are two main groups of neutron scattering techniques: elastic and inelastic. Elastic techniques are typically used to examine the structure, but inelastic techniques are used to probe the lattice dynamics of the materials under investigation. In contrast to the latter group, the former does not suggest that energy is exchanged between the sample's atoms and neutrons.

Powder Neutron Diffraction (PND) is a technique used to investigate the atomic arrangements and microstructure of powdered polycrystalline materials, as well as to detect and identify crystalline phases and quantitatively measure their lattice parameters and volume fractions. Brown used PND to study Ni_2MnGa Heusler alloy for Martensitic Transformation (MT) phase diagram determination **(Río-López et al., 2021)**. The existence of extensive quasielastic scattering across the magnetic transition is revealed by inelastic neutron scattering in La ($Fe_{13-x}Si_x$), and it is ascribed to spin fluctuations **(Morrison et al., 2024)**. $Zr_{1/3}Nb_{1/3}Hf_{1/3}$ HEA samples were made in both thin film and bulk forms; neutron scattering studies indicate that the bulk sample and thin film sample are in the b.c.c. phase **(Guo et al., 2012)**. Single Crystal Neutron Diffraction (SCND) measures the coherent scattering intensities (Bragg intensities) from a single crystal so that the crystal structure of the material can be analyzed. The positions of the atomic nuclei, unit cell site occupancies, and space group can be obtained using this method **(Río-López et al., 2021).** Glavatskyy used the SCND technique to study the Cu doping effect on the crystal structures of NiMnGaCu **(Glavatskyy et al., 2007)**.

CHAPTER FOUR

COMPARATIVE ANALYSIS OF MAGNETOCALORIC MATERIALS

The Ni_2–Mn-X-based Heusler alloys (H•A•s) (particularly for X = In or Sn), $La(Fe,Si)_{13}$ alloys, and HEAs are the current trends in magnetocaloric materials research, according to Law et al. (2023). This is because of their magnetocaloric properties and the fact that they are composed of abundant elements. The magnetocaloric effect and magnetic properties of these materials will be discussed in the following sections, along with a comparison of these materials based on their synthesis process, annealing time, and doping effect.

4.1 Ni_2MnX-based Heusler Alloy

4.1.1 Crystal and Magnetic structure of intermetallicNi_2–Mn-X-based Heusler alloys

Ni_2-Mn-X is called full Heusler because its chemical representation has the form X_2YZ, and its crystal structure is face-centered cubic with $L2_1$ phase, as shown in figure 4.1 & table 4.1. Where the elements X and Y are magnetic (transition metals), but Z is nonmagnetic (main group elements, Z = Al, Ga, In, Sn, and Sb) **(Asli et al., 2021; Ghahremani, 2014)**. The space group is Fm-3m with the coordinates A (0, 0, 0), B ($\frac{1}{4}, \frac{1}{4}, \frac{1}{4}$), C ($\frac{1}{2}, \frac{1}{2}, \frac{1}{2}$), and D ($\frac{3}{4}, \frac{3}{4}, \frac{3}{4}$) **(Ahn, 2024)**. These four interpenetrating sub lattices of fcc are filled by X elements, constructing a simple cubic lattice, but Y and Z exist in the centers **(Vinod et al., 2024)**.

When changing the concentrations of the carriers in full Heusler, a transition from the ferromagnetic phase to an antiferromagnetic phase occurs **(Kulkova et al., 2006).** Ni_2-Mn-X shows a giant magnetocaloric effect (GMCE) due to its magneto structural martensitic transformation (first-order transition) when cooling from austenite to martensite. Therefore,

these materials are candidates to become a promising future for cooling devices. Hence, the intrinsic brittleness and the wide thermal hysteresis must be overcome **(Ahn, 2024)**.

Table 4.1 The crystal structure and the magnetic order of Heusler alloys

X	Y	Z	Crystal structure	Magnetic order
Ni	Mn	Al, Ga, In, Sn, Sb	$L2_1$	FM

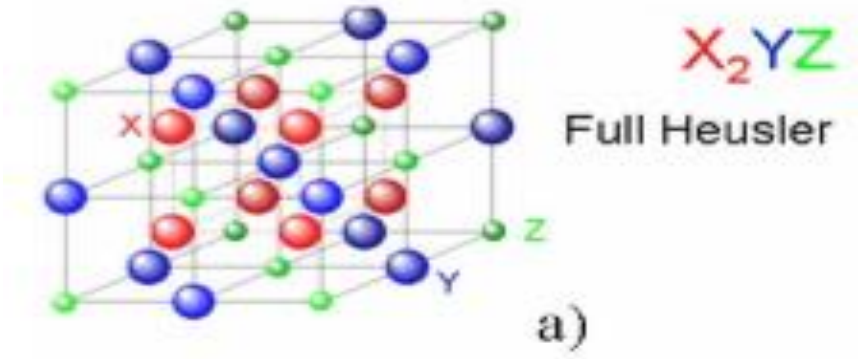

Figure 4.1 The structure of full Heusler with $L2_1$ phase **(Ghahremani, 2014).**

4.1.2 Ni_2MnGa

4.1.2.1 Magnetization measurement of Ni_2MnGa nanowires

According to a study by Zhang et al. to analyze the magnetocaloric, magnetic, and structure properties of Ni_2MnGa Heusler alloy nanowires, the sample has been prepared by the electrospinning method followed by optimized heat treatments. This was done by adding polyvinyl alcohol (PVA) to deionized water and then stirring the solution in a magnetic field to obtain a clear solution. Then Ni, Ma, and Ga 2:1:1 molar ratios were added and stirred in a magnetic field for three hours and then annealed in a furnace at a temperature from 873 K to 1073 K. The magnetic measurement (isothermal magnetization) performed by using the

(PPMS) with the (VSM) option applying a magnetic field up to five T. As shown in figure 4.2 the field-dependent magnetization M(H) of the nanowire measure with temperature range from 150 K to 350 K, in addition the figure divided into two regions a) represented nanowire sample annealed at 973K b) represented nanowire samples annealed at 1023 K. The magnetic entropy change was determined by the researchers (Zhang et al.) using Maxwell's relationship. It is theoretically possible to compute magnetic entropy using Maxwell's formulas. However, specific heat measurements are a direct approach to measuring magnetic entropy change because of experimental advantages.

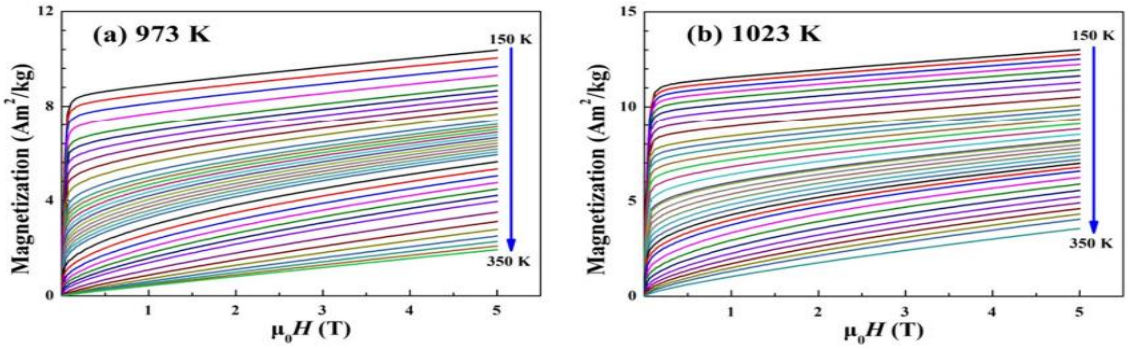

Figure 4.2 Isothermal magnetization measurements of Ni_2MnGa nanowires annealed at (a) 973 K and (b) 1023 K for 3 h measured from 150 K to 350 K **(Zhang et al., 2020)**.

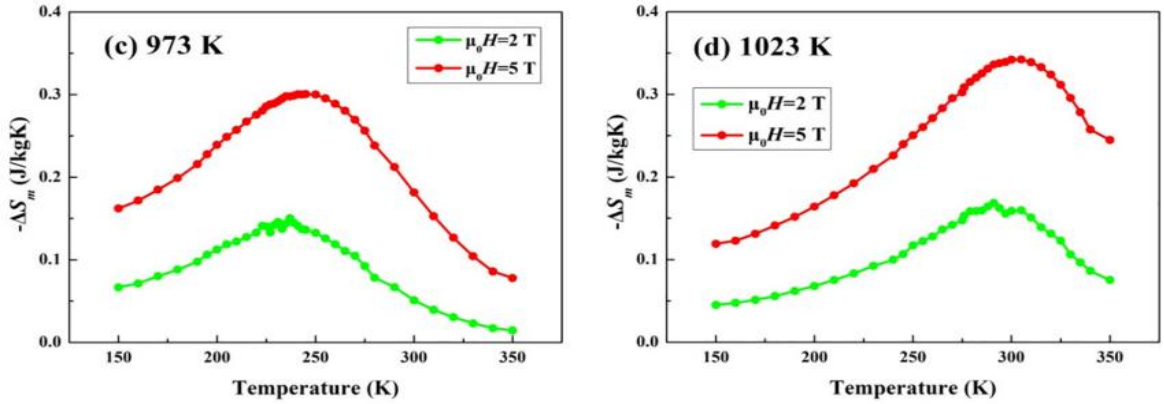

Figure 4.3 displays the temperature-dependent magnetic entropy change $-\Delta S_m$ of nanowires annealed at 973 K and 1023 K in magnetic fields of 2 T and 5 T, (c) and (d), respectively.

The highest magnetic entropy change, ΔS_m^{peak}, with an applied field of 5 T is 0.30 J/kgK at 973 K and 0.35 J/kgK at 1023 K. This suggests that as the annealing temperature rises, so does the

maximum magnetic entropy. Moreover, for applied field 5 T, the greatest values happen at 245 K for 973 K and 305 K for 1023 K. This suggests that room temperature magnetic cooling is more appropriate for the annealed nanowires at 1023 K.

The temperature-dependent magnetization M(T) was measured in a magnetic field of 200 Oewith temperature varied at a constant rate of 1 K/min for all nanowire samples, as shown in figure 4.4. The magnetic moment increases rapidly (continuously) with decreasing temperature, which means that the nanowires have a ferromagnetic phase. As can be seen in figure 4.4, the Curie temperature T_c computed from the $\frac{dM}{dT}$ versus T curves is equivalent to 235 K for samples annealed at 973 K and 288 K for samples annealed at 1023 K. The higher Curie temperature is caused by a greater exchange interaction.

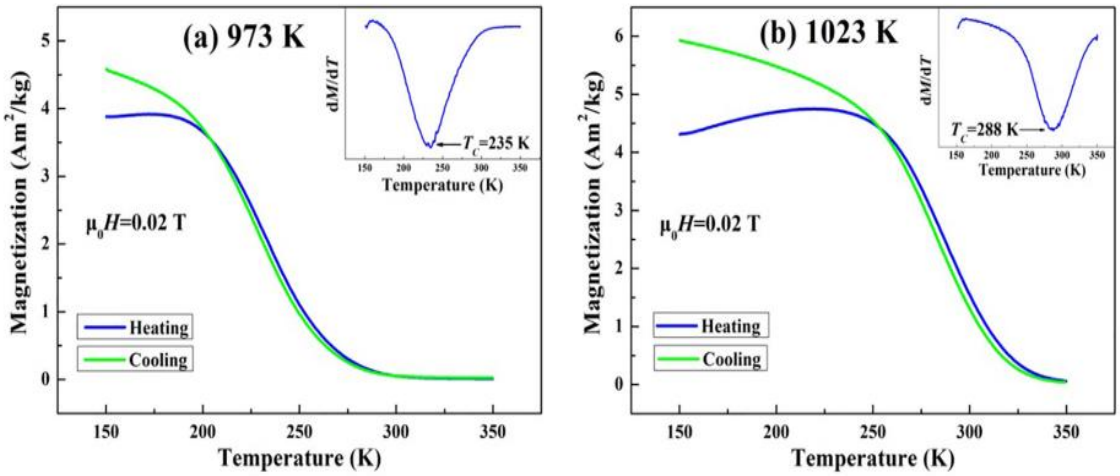

Figure 4.4 M-T curves of the nanowire samples under various heat treatment conditions: (a) 973 K and (b) 1023 K annealed for 3 h. Insets show the dM/dT-T curves from which the Curie temperature T_c was calculated **(Zhang et al., 2020)**.

The χ^{-1} versus T for the 973 K annealed nanowires was plotted, as illustrated in figure 4.5, to investigate the mechanisms behind the magnetic transition in Ni_2MnGa nanowires. The Curie-Weiss temperature was determined by fitting a line in a paramagnetic region. Figure 4. 5 illustrates that the Curie-Weiss temperature, or x-intercept of the fitting line, is equal to the positive value 241 signifying the paramagnetic-ferromagnetic transition in the nanowires and is roughly equivalent to T_C = 235 K **(Zhang et al., 2020).**

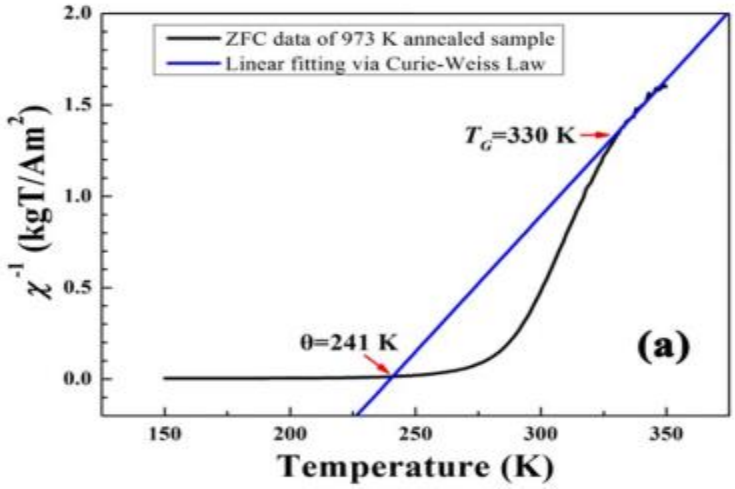

Figure 4.5 The Curie-Weiss fitting of the versus T curve of the Ni-Mn-Ga nanowire sample annealed at 973 K **(Zhang et al., 2020).**

Table (A-4.2) Role of the physical form on Curie transition temperature and on the maximum change in the magnetic entropy of different compositions of Ni-Ga-Mn alloys at a magnetic field change of about 5 T.

Alloy Composition	**Physical form**	$-\Delta S_m^{peak}$ **(J/kgK)**	**T_c (K)**	$\mu_0 H$**(T)**	**Reference**
Ni_2MnGa	Nanowires	0.35	305	5	**(Zhang et al., 2020)**
$Ni_{55}Mn_{20}Ga_{25}$	Bulk (Single crystal)	86	313	5	**(Pasquale et al., 2005)**
$Ni_{55.2}Mn_{18.6}Ga_{26.2}$	Bulk (Polycrystalline)	20.4	317	5	**(Zhou et al., 2004)**
$Ni_{52}Mn_{26}Ga_{22}$	Thin Ribbons	30	-	5	**(Z. Li et al., 2014)**

Table (B-4.2) Role of the physical form on Curie transition temperature and on the maximum change in the magnetic entropy of different compositions of Ni-Ga-Mn alloys at a magnetic field change of about 5 T.

$Ni_{57.25}Mn_{22.25}Ga_{20.5}$	Bulk (Polycrystalline)	20	-	5	**(Z. Li et al., 2014)**
$Ni_{50.95}Mn_{25.45}Ga_{23.6}$	Glass-Coated Microwires	0.7	315	5	**(Varga et al., 2011)**
Ni-Mn-Ga-Cu	Microwires	8.3	-	5	**(X. Zhang et al., 2016)**

Table 4.2 shows that the single crystal has the maximum magnetic entropy change value due to strong magnetocrystalline anisotropy **(Ke et al., 2016)**; nevertheless, practical applications like magnetic refrigeration are hampered by the single crystal's high cost because of low mass productivity (**Kusama et al., 2017)** and production complexity **(Li et al., 2014)**. Therefore, the polycrystalline bulk form is recommended, although Heusler-type bulk alloys are typically inherently brittle, making processing them challenging. Refrigerant alloys can now be produced in a single step with quick solidification by melts pinning as an alternative to traditional preparation **(Li et al., 2014)**. In addition, the change from micrometer to nanometer forms the maximum of the magnetic entropy drop from 0.7 J/kgK to 0.35 J/kgK at a magnetic-field change of 5 T. Therefore, the magnetic entropy change strongly decreases on reduction of sample size down to nanoscale due to the change of magnetostructural phase transition and magnetic homogeneity **(Zhang, Fan, et al., 2016)**, but the magnetic entropy change of the microwires can be enhanced by doping, as seen in Ni-Mn-Ga-Cu**,** and the nanowires can also be enhanced 10–15 times by doping or by changing the atomic ratio of Ni to Mn **(Zhang et al., 2020).** There is also a significant magnetic entropy change in the thin ribbon. Additionally, table 4.2 demonstrates that the nanowires' Curie temperature is lower than that of the bulk and glass-coated microwires due to the fact that, when compared to bulk materials, nanomaterials have a higher surface-to-volume ratio, which means a large number of atoms are at the surface or near it, The surface atoms have neighbors only in one side, so

they have less neighbor atoms and easy to get effected by the thermal fluctuations. Results in weakening of exchange interactions and finally a reduction in Curie temperature **(Zhang et al., 2020)**.

4.1.3 Ni_2MnSn

According to a study by Bhatt et al., a polycrystalline bulk ingot of Ni_2MnSn was made utilizing a solid-state reaction technique in order to investigate the magnetic characteristics of Ni2MnSn-based Heusler alloy. The appropriate stoichiometric ratio was achieved by combining high-purity elemental powders (Ni, Mn, and Sn). A hydraulic press was then used to form the mixture into a rectangular pellet, which was then enclosed in an evacuated quartz tube and subjected to a vacuum of around 10^{-5}mbar. After that, the sealed tube was annealed for 15 days at 1050°C to guarantee a uniform and stable phase. In order to maintain the high-temperature phase, the sample was lastly quenched in ice water. A powder X-ray diffractometer was used to characterize the sample at room temperature, whose analysis revealed the presence of the full Heusler austenite cubic structure (space group Fm-3m, no. 225), and the Rietveld refinement method was used to calculate the lattice parameter, which is equal to $6.035A^0$**.**The isothermal magnetization M(H) or magnetic field-dependent magnetization, as measured by SQUID (superconducting quantum interference device) magnetometry, is depicted in figure 4.6 at 5 K and 300 K. The material exhibits soft ferromagnetic properties, as confirmed by the observed fast rise in magnetization and weak hysteresis. The saturation magnetization drops with temperature, which is consistent with a change from a ferromagnetic to a paramagnetic state **(Bhatt et al., 2024)**.

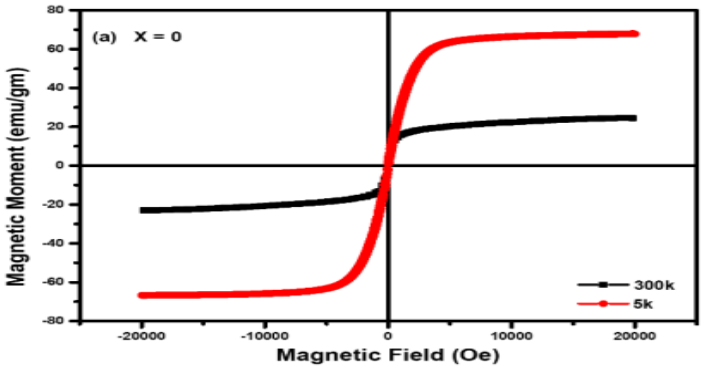

Figure 4.6 The M versus H curves of Ni_2MnSn at 300K and 5K **(Bhatt et al., 2024)**.

Table 4.3 shows the influence of different Sn concentrations on magnetization in as-melted and annealed $Ni_{50}Mn_{50-x}Sn_x$ alloys (Dan et al., 2014).

Composition $Ni_{50}Mn_{50-x}Sn_x$	Synthesis method	Annealing temperature (k)	Annealing time	Magnetization at room temperature (emu/g)	$\mu_0 H_{5T}$ (T)
X=10	Arc melting	1123.15	4h	Near zero	5
X=15	Arc melting	1123.15	4h	Above 30	5
X=20	Arc melting	1123.15	4h	40	5
X=30	Arc melting	1123.15	4h	37	5
X=40	Arc melting	1123.15	4h	Below 10	5

Table 4.3 shows the alloy compositions of $Ni_{50}Mn_{50-x}Sn_x$ (x=0, 11, 12, 13, 14, 15, 16, 17, 18, 19, 20, 30 and 40) that were created using the arc melting process. The magnetic characteristics of the samples were examined using pulsed fields and vibrating sample magnetometers. When magnetization is carried out at room temperature and a magnetic field of 5 T, it grows with X until it reaches its maximum at X=20, at which point it starts to drop. This means that as the concentration of Sn increases, magnetization increases, and after X=20, it starts to decrease. This is because of the atoms' exchange interaction inside the alloys, which has the potential to affect the saturation magnetization and curie temperature of ferromagnetic alloys by making them stronger or weaker **(Dan et al., 2014)**.

The Ni-Mn based Heusler alloys show abrupt change in the magnetization due to a first order magnetostructural transition from austenitic ferromagnetic phase to a low magnetization

martensite phase, where the structural transition induces latent heat change and the magnetic transition induces entropy change, the magnetocaloric effect and transformation temperature of these alloys can be induced by doping with Cu, Ga, Sb, C, Fe, Co and Al as seen in table 4 **(Cicek et al., 2020; Kavita et al., 2019).**

We shall talk about the impact of boron doping at the Sn location. The atomic radius of boron is tiny, and it is nonmagnetic. With the B doping $Ni_{43}Mn_{47}Sn_{10.5}B_{0.5}$, the martensite transition temperature (T_m) of $Ni_{43}Mn_{47}Sn_{11}$ rises from 210K to 280K. Researchers typically attribute temperature changes T_m like this to changes in valence electron concentration to atom ratio (e/a) when composition variations or atomic substitution. However, in this particular case of B doping, where the valence electron of B ($2s^2\ 2p^1$) is less than that of Sn ($5s^2\ 5p^2$), they attribute the temperature change to lattice expansion. In summary, the e/a ratio or the cell volume can alter the change in T_m **(Kavita et al., 2019; Xuan et al., 2008)**. Additionally, as can be seen in Table 4.4, the ΔS_m^{peak} of $Ni_{43}Mn_{47}Sn_{10.5}\ B_{0.5}$ is 22 J/kgK larger than that of $Ni_{43}Mn_{47}Sn_{11}$ because of i) the magnetostructural transition and ii) the large magnetization difference (32 Am^2/kg) between As (austenite start temperature) and A_f (austenite final temperature) in the B-doped sample's isotherms. This is due to the enhanced magnetostructural coupling caused by lattice modification, as the lattice contracts with B-doping, resulting in a decrease in the Mn-Mn distance in the lattice. The exchange interaction is ascribed to the spontaneous structural transition that occurs in conjunction with the magnetic transition in Ni-Mn-based Heusler alloys, where the magnetic moments are primarily localized on the Mn atoms; (iii) field-induced structural phase transition from the low magnetic martensite phase to the high magnetic austenite phase and sharpness of metamagnetic transition **(Kavita et al., 2019)**.

The impact of Si concentration on the magnetic entropy change and transition temperatures, including the austenite phase's Curie transition (T_C) and martensitic transition (T_m), was investigated by Kumar et al. Table 4.4 shows that the T_c and the T_m decrease when the Si concentration of $Ni_{47}Mn_{40-x}Si_xIn_{13}$ rises from x = 1 ($Ni_{47}Mn_{39}Si_1In_{13}$) to x = 3 ($Ni_{47}Mn_{37}Si_3In_{13}$) at applied field 0.05 T. As previously stated, the decreases in T_m are ascribed to the decreases in the e/a valence electron concentration to atom ratio **(Kumar et al., 2020)**.

However, the decreases in T_c are caused by the fact that the magnetic moment localizes on the Mn atoms, and as a result, the concentration of the magnetic moment decreases when the Mn atoms are replaced with the Si **(Khovailo et al., 2004)**. The greater magnetization of the sample in the isothermal curves from FM interactions between Mn-Mn atoms that occur in these alloys ($Ni_{47}Mn_{40-x}Si_xIn_{13}$) causes the maximum magnetic entropy change to rise when the Si concentration increases from x= 1 to x = 3 **(Kumar et al., 2020)**.

Because of the higher change in magnetization throughout the martensitic transition in the $Ni_{50}Mn_{34}In_{16}$ alloy compared to the $Ni_{50}Mn_{34}Sn_{16}$ alloy, the ΔS_m^{peak} of $Ni_{50}Mn_{34}In_{16}$ is bigger than that of $Ni_{50}Mn_{34}Sn_{16}$. This is most likely because the martensitic transition and the Curie temperature of the ferromagnetic martensite phase of NiMnIn are located in the same temperature range. Moreover, the NiMnIn alloy exhibits a greater field-induced martensite to austenite transition than the NiMnSn alloy **(Sharma et al., 2007)**.

Table (A-4.4) shows the synthesis method, annealing temperature, annealing time, Curie transition (T_C), martensitic transition (T_m), and the maximum change in the magnetic entropy ΔS_m^{peak} (J/kgK) of different compoundsof the Ni-Mn-based Heusler alloys:

Composition	Synthesis method	Annealing Temperature (k)	Annealing time	ΔS_m^{peak} (J/kg K)	T_m (k)	T_c (K)	$\mu_0 H$ (T)	Reference
$Ni_{47}Mn_{39}Si_1In_{13}$	Arc melting	1173.15	6 h	12.3 For 2 T	299 For 0.05 T	302 For 0.05 T	0.05 & 2	**(Kumar et al., 2020)**
$Ni_{47}Mn_{37}Si_3In_{13}$	Arc melting	1173.15	6 h	30.6 For 2 T	238 For 0.05 T	260 For 0.05 T	0.05 & 2	**(Kumar et al., 2020)**

Table (B-**4.4**) **shows the synthesis method, annealing temperature, annealing time, Curie transition (T_C), martensitic transition (T_m), and the maximum change in the magnetic entropy ΔS_m^{peak} (J/kgK) of different compoundsof the Ni-Mn-based Heusler alloys:**

$Ni_{43}Mn_{47}Sn_{10.5}B_{0.5}$	Arc melting	1173	72 h	22	280	283	5	**(Kavita et al., 2019)**
$Ni_{43}Mn_{47}Sn_{11}$	Arc melting	1173	72 h	17	210	267	5	**(Kavita et al., 2019)**
$Ni_{50}Mn_{34}In_{16}$	Arc melting	1073.15	2 h	19	220	305	8	**(Sharma et al., 2007)**
$Ni_{50}Mn_{34}Sn_{16}$	Arc melting	1273.15	24 h	2	220	306	8	**(Sharma et al., 2007)**

Table (A-4.5) shows the synthesis method, annealing temperature, annealing time, the maximum change in the magnetic entropy of different compounds of the Ni-Mn-based Heusler alloys at a magnetic field change of about 5 T:

Composition	**Synthesis method**	**Annealing Temperature (K)**	**Annealing Time (h)**	**ΔS_m^{peak} (J/kg K)**	**$\mu_0 H$ (T)**	**Reference**
$Ni_{48}Ag_2Mn_{37}In_{13}$	Arc melting	1173	24	15.2	5	**(S et al., 2023)**
$Ni_{41}Mn_{43}Sn_{10.0}Co_6$	Induction melting	1173	24	29.5	5	**(X. Zhang et al., 2018)**
$Ni_{43}Mn_{45.0}B_{1.0}In_{11}$	Arc melting	1073	120	25.06	5	**(Saritaş et al., 2023)**

Table (B-4.5) shows the synthesis method, annealing temperature, annealing time, the maximum change in the magnetic entropy of different compounds of the Ni-Mn-based Heusler alloys at a magnetic field change of about 5 T:

$Ni_{50}Mn_{35}In_{13.9}B_{1.1}$	Arc melting	1123.15	24	16	5	**(Pandey et al., 2017)**
$Ni_{50}Mn_{34}B_{1}In_{15}$	Arc melting	1073	168	15	5	**(Cicek et al., 2020)**
$Ni_{50}Mn_{33.5}B_{1.5}In_{15}$	Arc melting	1073	168	8	5	**(Cicek et al., 2020)**

Table 4.5 shows the ΔS_m^{peak} of $Ni_{43}Mn_{45.0}B_{1.0}In_{11}$ is 25.06 J/kgK **(Saritaş et al., 2023)**, which is comparable with other Ni-Mn based alloys at 5 T such as 29.5 J/kgK for $Ni_{41}Mn_{43}Sn_{10.0}Co_6$ **(Zhang et al., 2018)**, 15.2 J/kgK for $Ni_{48}Ag_2Mn_{37}In_{13}$ **(Set al., 2023),** 16 J/kgK for$Ni_{50}Mn_{35}In_{13.9}B_{1.1}$ **(Pandey et al., 2017),** 15 J/kgK for $Ni_{50}Mn_{34}B_1In_{15}$**,** and 8 J/kgK for $Ni_{50}Mn_{33.5}B_{1.5}In_{15}$ **(Cicek et al., 2020).**

4.2 $La(Fe,Si)_{13}$ alloys

4.2.1 Crystal and magnetic structure of intermetalic $La(Fe,Si)_{13}$ alloys

$La(Fe,Si)_{13}$ alloys are also candidates to become the promising future for cooling devices due to their giant magnetocaloric effect in the magnetic phase transition between ferromagnetism and paramagnetism and T_C around 200 K **(Song et al., 2024)**. $La(Fe,Si)_{13}$compounds are the first example realizing the itinerant-electron metamagnetic transition from the paramagnetic to the ferromagnetic state **(Fujita, Fukamichi, et al., 2003)**, they consist of abundant, cheap, and non-toxic elements. Hence, the curie temperature must be adjusted near the room temperature. It is also a ferromagnetic alloy **(Paul-Boncour & Bessais, 2021)**, with a cubic $NaZn_{13}$-type crystal structure and space group Fm-3cas shown in Figure 4.7 **(Vinod et al., 2024)** or tetragonal $Ce_2Ni_{17}Si_9$- type structure **(Paul-Boncour & Bessais, 2021)**.

According to Long et al. (2024), the sample was prepared by induction melting or arc melting

by putting it in quartz tubes in a vacuum, annealed at 1,323 K for no fewer than five days, and quenched in freezing water **(Long et al., 2024).**

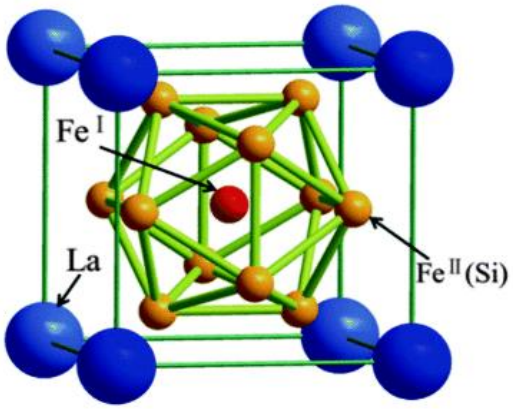

Figure 4.7 The crystal structure of $La(Fe,Si)_{13}$ alloys, where Fe occupies the whole 8b site, Fe and Si collaborate on the 96i site, and the 8a site occupies by La **(Vinod et al., 2024)**.

4.2.2 $LaFe_{13-x}Si_x$ alloys (X=1.4, 1.6, 1.8, 2)

Phejar et al. (2011) found that a very short treatment annealing time (30 minutes) was required to obtain a well-crystallized 1:13 phase in all $LaFe_{13-x}Si_x$ compounds from the amorphous phase where the α-(Fe,Si) existed. The study focused on $LaFe_{13-x}Si_x$ alloys with X = 1.4, 1.6, 1.8, and 2. The samples were synthesized by ball milling. PPMS was used to measure the magnetocaloric and magnetic characteristics between 1.9 and 350 k and up to 9 T. Because the Si atomic radius ($1.322A^0$) is greater than the Fe atomic radius ($1.274\ A^0$), the researchers expect that the lattice parameter a will likewise grow as the Si content increases. However, the XRD reveals that the cell parameter remains unchanged with Si concentration, indicating that the interatomic distance from the atomic locations and lattice parameter are composition-independent this is attributed to the amount of Si remains small compared to the Fe. Due to the Si atoms located at 96i sites, all Fe atoms in $La(Fe,Si)_{13}$ have Si atoms as their nearest neighbors at an interatomic distance of approximately 2.457Å. This configuration leads to a shift in the Curie temperature (T_c), which increases from 200.2 K to 228.5 K as the Si concentration (x) rises from 1.4 to 2 **(Tegus et al., 2002)**. The increase in T_c with Si substitution can be attributed to the modification of the electronic structure, particularly by

increasing the density of states at the Fermi level. This enhancement favors ferromagnetic ordering according to the Stoner criterion, which indicates that ferromagnetism occurs when the product of the DOS at the Fermi level and the exchange interaction parameter (I) exceeds a critical value **(Fujita, Fujieda, et al., 2003)**. Thus, the increased DOS promotes itinerant ferromagnetism and drives up T_c. Additionally, the presence of Si as a nearest neighbor to Fe leads to Fe-Si hybridization, where the 3d orbitals of Fe overlap more strongly with the 3p orbitals of Si. This hybridization redistributes electron density around Fe atoms and stabilizes magnetic ordering by optimizing the electronic environment **(Wen et al., 2002)**. Although the Fe-Fe distance increases with Si doping weakening direct Fe-Fe exchange interactions, the Fe-Si hybridization and enhanced DOS compensate for this reduction, ultimately stabilizing the ferromagnetic phase and contributing to the increase in Curie temperature.

The temperature-dependent magnetization M(T) of the $LaFe_{11.4}$ $Si_{0.6}$ was measured in a magnetic field of 0.01 T with temperature varied at a constant rate of 4 K/min, as shown in figure 4.8. The sharp change in magnetization and the thermal hysteresis of 7.5 K indicating a (FOMT), the magnetic saturation is M_S=181.0 $Am^{2/}kg$ at 2 K under 2 T, which not change even though the applied field increase from 2T to 9T .

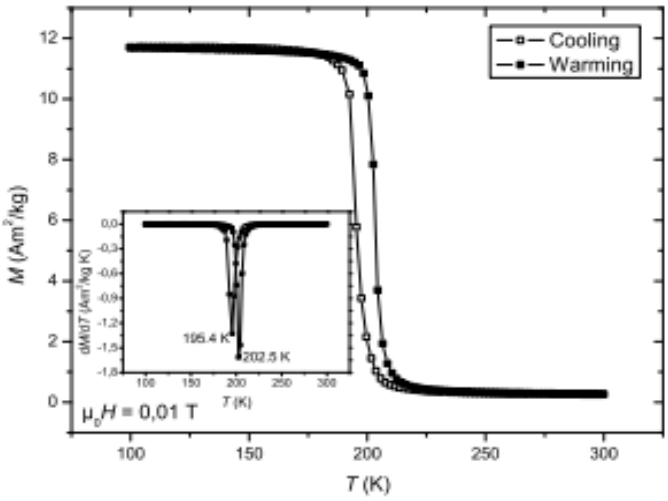

Figure 4.8 The M(T) curve of $LaFe_{11.4}$ $Si_{0.6}$ in magnetic field 0.01 T **(Phejar et al., 2011)**.

A collection of M (H) curves around the Curie temperature, in the 169–250 K temperature range with a 3 K temperature step, and in the 0–5 T magnetic field range are depicted in

figure 4.9. At X = 1.4 and 1.6, the magnetization curves exhibit a (FOMT) from paramagnetic to ferromagnetic; however, at X = 1.8 and 2, the curves drop more slowly, resulting in a magnetic transition that is (SOMT) **(Phejar et al., 2011)**.

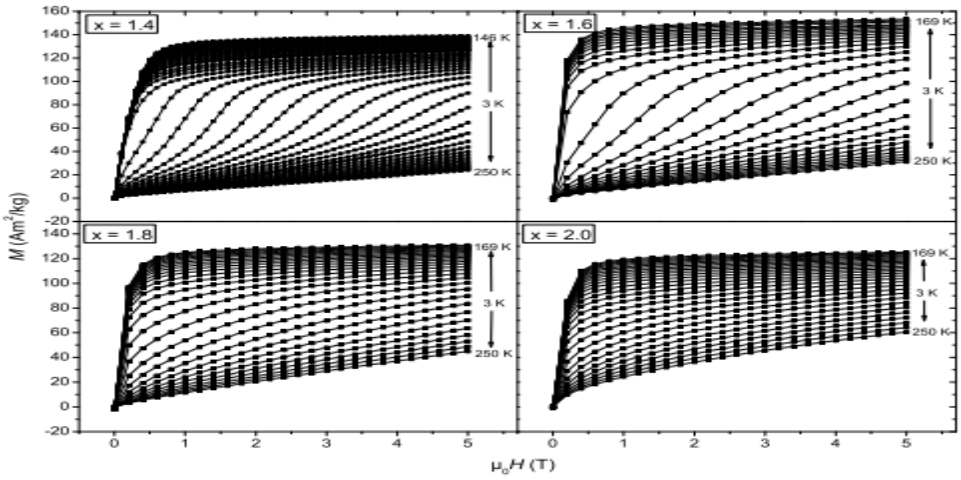

Figure 4.9 M(H) curves of the $LaFe_{13-x}$ Si_x compounds. The curves were measured by decreasing the temperature from 169K to 250K and increasing the magnetic field from 0 to 5T in the vicinity of T_C **(Phejar et al., 2011)**.

The peritectic interaction of the solid phase α-(Fe,Si) and liquid phases (La-rich) creates the 1:13 phase of $La(Fe,Si)_{13}$ alloys. The resultant phases are LaFeSi, α-(Fe,Si), and a minor quantity of the single-phase $NaZn_{13}$ because of non-equilibrium solidification behavior. Due to the solid state diffusion process, a significant number of primary Fe-Si dendrites that are produced during the annealing process may react with the La-rich phase to form the 1:13 phase.$LaFe_{13-x}$ Si_x compounds can be manufactured using a variety of methods, including melt spinning, arc melting, ball milling, and induction melting. Table 4.6 displays the melt's annealing time for different synthesis methods of the $La(Fe,Si)_{13}$ alloy. Compared to arc melting, spinning (rapid solidification) and ball-milling (mechanical alloying) are less. In order to achieve stress relief, grain refinement, and an almost single phase $NaZn_{13}$ structure in the samples, arc-melted materials usually require longer annealing durations (sometimes several hours to days) due to slower cooling rates that result in larger grain sizes. However, because ball milling produces fine particles, which are small grains, the annealing process can proceed more quickly because to the finer particles and increased fault density. Because of

the material's previously refined structure from milling, it can attain its required qualities more quickly. In the melt spinning used for the production of $La(Fe,Si)_{13}$ ribbons, which is a rapid cooling synthesis, the grain size is smaller. The alloys created using this method don't require more time to anneal due to shortening the diffusion path, and they have a higher Currie temperature. $LaFe_{11.27}$ $Si_{1.43}$ exhibits a Curie temperature of 192 K in bulk alloys and 210 K in ribbons of the same composition. Because of the fast rate of cooling, materials of the melt-spun type dissolve more silicon in the 1:13 phase. As previously stated, the table also demonstrates that the Curie temperature rises with Si doping **(Paul-Boncour & Bessais, 2021; Phejar et al., 2011; Vinod et al., 2024).**

Table 4.6 The role of different synthesis methods on annealing time and curie temperature of different compounds of the $LaFe_{13-x}Si_x$ alloys:

Composition	Synthesis method	Annealing temperature (k)	Annealing time (h)	T_C (k)	References
$LaFe_{11.3}Si_{1.7}$	Arc melting	1423	720.5	228.5	**(Phejar et al., 2011)**
$LaFe_{11.4}Si_{1.6}$	Arc melting	1273	720	209	**(Shen et al., 2009)**
$LaFe_{11.5}$ $Si_{1.5}$	Arc melting	1323	300	205	**(Hou et al., 2015)**
$LaFe_{11.6}Si_{1.4}$	Arc melting	1573	1	190	**(Liu et al., 2009)**
$LaFe_{11.6}Si_{1.4}$	Arc melting	1373	24	202	**(Peng et al., 2020)**
$LaFe_{11.7}Si_{1.3}$	Arc melting	1323	1200	188	**(Hu et al., 2003)**
$LaFe_{11.8}Si_{1.2}$	Arc melting	1373	720	186	**(Ipus et al., 2017)**
$LaFe_{11.6}Si_{1.4}$	Ball-milled	1373	0.5	200.2	**(Phejar et al., 2011)**
$LaFe_{11}Si_2$	Ball-milled	1373	0.5	228.5	**(Phejar et al., 2011)**
$LaFe_{11.5}Si_{1.5}$	Melt- Spinning	1300	5	195	**(Xie et al., 2004)**
$LaFe_{11.8}Si_{1.2}$	Melt–Spinning	1323	2	195	**(Gutfleisch et al., 2005)**
$LaFe_{11.6}Si_{1.4}$	Melt-Spinning	1323	0.5	223	**(Hou et al., 2015)**

4.2.3 Adjusting the Curie temperature of La(Fe Si)$_{13}$-based alloys

In La(Fe,Si)$_{13}$-based alloys, the Fe-Fe interbond distances, magnetic exchange coupling, and lattice parameters can be adjusted to change MCE and T_C by partially substituting La with elements such as Ce and Pr**(Song et al., 2024)**, and by partially substituting Fe with elements like Ni and Co **(Md Din et al., 2013; Xian et al., 2023; Zong & Long, 2017)**, or by doping with the light elements such as C, H, or combination of both **(Paul-Boncour & Bessais, 2021)**. For example, as illustrated in figure 4.10, Song et al. found that when doping La(Fe,Si)$_{13}$ with Al, the Curie temperature rises as the Al content increases. This is initially explained by the fact that in itinerant ferromagnets (La(FeSi)$_{13}$), magnetic properties originate from the conduction electrons rather than from localized atomic moments **(Zwerger, 2009)**. The energy band (3d band) narrows as the Fe-Fe interatomic distance increases with Al doping, causing itinerant electrons to become more localized and have lower kinetic energy. This facilitates the exchange interaction's ability to overcome the kinetic energy, favoring parallel spin alignment. So that the Fe atoms align more readily as a result of improved exchange contact, increasing the exchange splitting and raising the Curie temperature **(Al-Zubi, 2010; Song et al., 2024)**.

In the case of the $LaFe_{11.31}$ $Si_{1.69}$ $H_{1.45}$ alloy, the Stoner-type exchange interaction is the primary type responsible for the ferromagnetic behavior. As hydrogen is introduced, it expands the lattice and increases the Fe-Fe distance. This reduces the kinetic energy of the itinerant electrons (due to decreased overlap between Fe orbitals) and narrows the energy bands. With a narrower band, the Stoner criterion $I\, n(E_F) > 1$ is easily applicable, so the exchange splitting can increase, enhancing the Curie temperature as the Fe atoms align more easily due to enhanced exchange interaction **(Al-Zubi, 2010; Rosca et al., 2010).**

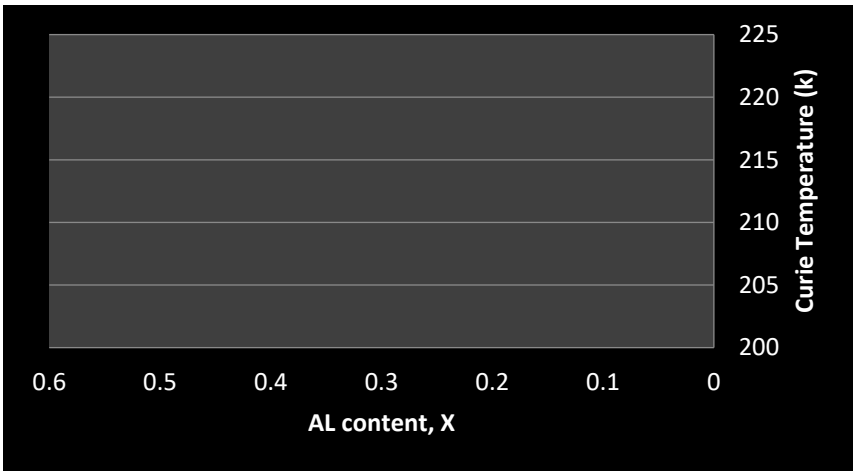

Figure 4.10 Effect of Al content (X = 0.1–0.5) on the Curie temperature, the data taken from reference **(Song et al., 2024).**

4.3 High Entropy Alloys

4.3.1 Crystal and Magnetic structure of HEAs

High-entropy alloys (HEAs) have four or more primary elements, with each component's own alloying concentration ranging from 5 to 35 atomic percent **(Foadian et al., 2023).** They appeared and formed in 2004 **(Koblischka & Koblischka-Veneva, 2022)** by Yeh et al. **(Yeh et al., 2004)** and Cantor et al. **(Cantor et al., 2004)**. Alloys with radiation resistance, corrosion, and excellent mechanical properties **(Law & Franco, 2023)**. HEAs are also current trends in research because of their remarkable and appealing combination of structural, chemical, physical, or magnetic properties. A HEA that shows magnetic properties is called a magnetic high-entropy alloy. But there are some HEAs that show magnetic properties at low temperatures but not at room temperature. HEA is considered a broad science, but only a small part of it has been studied **(Chaudhary et al., 2021).** If the configurational entropy $\Delta S_{mix} \geq 1.5$ R (where R is the gas constant), the alloys are regarded as HEAs **(Panwar, 2018)**.

At first, the high-entropy alloys consist of five or more elements in equiatomic proportions as single-phase, solid-solution metallic alloys. But the concept has expanded to encompass a wider range of materials, like non-equiatomic compositions, enabling exploration of a wider

range of element combinations and properties. Additionally, the focus has expanded to include intermetallic materials, materials with four or more principal elements, microstructures comprising various types and numbers of phases, and ceramic compounds. Other names, such as high-entropy materials (HEMs) and complex concentrated alloys (CCAs), have been developed to account for this wider breadth **(Law & Franco, 2022)**.

There are different crystal structures of HEA, for example, the bcc-type structure, which is also called type-A HEA (e.g., NbTaTiZrSiGe and also when Zr has been substituted with U), the α-Mn structure, which is called type-B HEA (such as $(ZrNb)_{0.1}(MoReRu)_{0.9}$), and the hcp structure, which is called type-D structure (like $Re_{0.56}Nb_{0.11}Ti_{0.11}Zr_{0.11}Hf_{0.11}$) (see figure 4.11) for the different structures of HEA alloys **(Koblischka&Koblischka-Veneva, 2022).**

The low coercivity (H_C) and high saturation magnetization (M_s) properties can be found in HEA, such as$FeCoNiAl_{0.2}Si_{0.2}$ and $FeCo_xNiAlCr_{1-x}$. These properties are dependent on the nature of the crystal structures of the phases and the elements in the alloy. The high saturation magnetization properties are considerably decreased with the replacement of Co with Cr in FeCoNi or by the addition of Al and/or Si. The elements (Co, Ni, and Fe) are ferromagnetic, but Al and FeCoCrNi are paramagnetic, but when adding Al to FeCoCrNi, it becomes ferromagnetic at room temperature. Also, the total exchange interactions, M_s and Tc, in FeCoNiMn or FeCoNiCr increase with the substitution of the non-magnetic element Cu in these alloys**.**

The task of knowing which elements can develop the magnetic properties of these alloys is not easy. Various studies in HEA have been done to adjust T_C at room temperature, including FeCoNiCu(X) (X = Pt, Mn, Mo, and Ag). The crystal structure of FeCoNiCr changes from FCC to BCC + FCC and then to BCC. By adding Al, it involves the creation of $L1_2$ and B2 phases.

When x increased from 0 to 2, $FeCoNi(MnAl)_x$ HEA transitioned from FCC to FCC + BCC combination, followed by a BCC phase. The phase structure of FeCoNiCrMn transitioned from FCC to HCP by using the processing procedures of atmospheric pressure and high pressure synthesis, respectively. Thus, the magnetic properties of HEA are affected by the alloy type, composition, synthesis route, and number of phases. Magnetic HEA is produced

by different techniques like melt spinning, mechanical milling, and arc melting, as seen in figure 4.12 **(Chaudhary et al., 2021).**

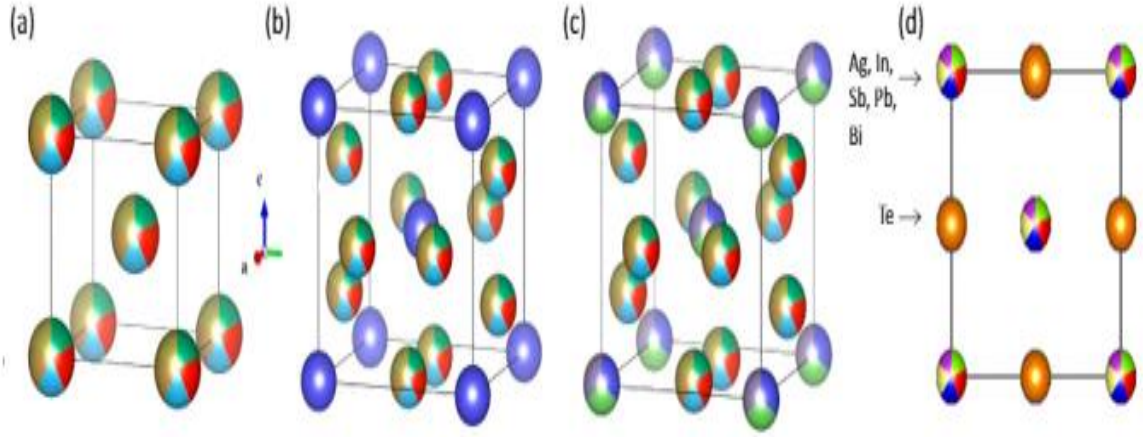

Figure 4.11 Different structures of HEA alloys: (a) BCC; (b) A15 structure (Cr_3Si-type), where the Si-site is occupied by HEA; (c) full A15 HEA. The mixed-color atoms indicate that the place is randomly inhabited. (d) HEA alloys with a cubic NaCl-type structure, where one (cationic) position fills with different metals in a shared fashion and the other (anionic) position is occupied only by Te **(Koblischka & Koblischka-Veneva, 2022)**.

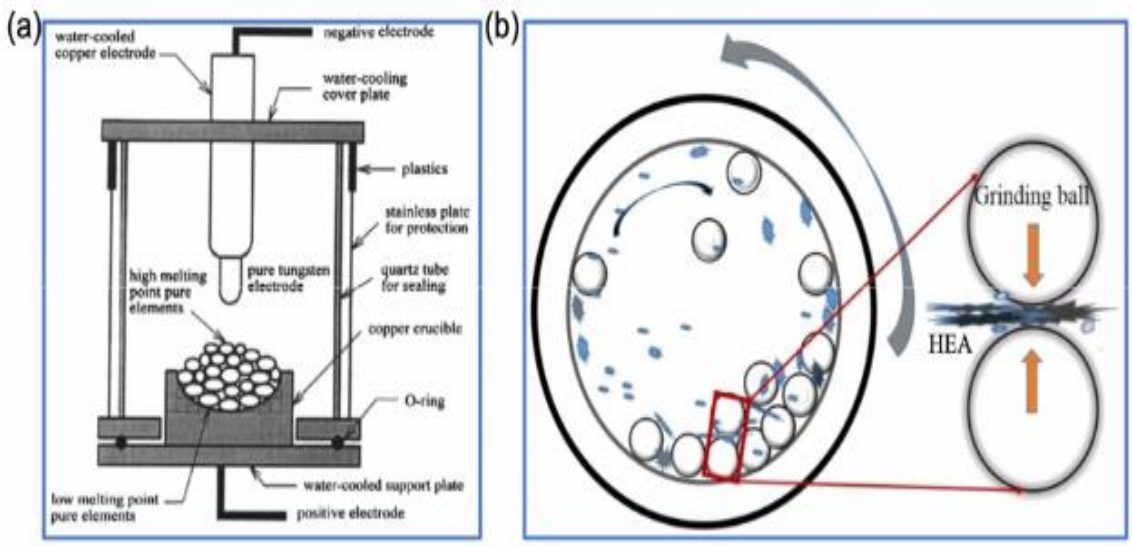

Figure 4.12 Schematic of (a) the arc melting technique and (b) the ball milling technique **(Chaudhary et al., 2021)**

4.3.2 The magnetocaloric effect and magnetic properties for different HEAs

The base alloy, alloying element additions, resultant phases, and their volume fractions all affect the HEAs' magnetic properties **(Panwar, 2018)**. According to table 4.7, non-magnetic elements like Mn, Ga, Al, and Sn can be added to equiatomic FeCoNiCr-based ferromagnetic high-entropy alloys with FCC structure to modify their magnetic behavior. This is typically followed by structural changes. When Al and Ga are added, they exhibit ferromagnetic behavior with the FCC and BCC structures; the BCC phase increases the ferromagnetic properties; at applied field 2 T, the curie temperature and saturation magnetization, which were 104 K and 0.5 emu/g for the based FeCoNiCr alloy, are increased to 703 K, 38 emu/g, and 277 K, 25 emu/g for FeCoNiCrGa and FeCoNiCrAl, respectively **(Na et al., 2017)**. The BCC phase of these high-entropy alloys tends to enable stronger magnetic alignment than the FCC phase; this could be because of the BCC's improved magnetic exchange contacts and reduced coordination. Also, because FCC structures are densely packed, spin alignment may be limited, resulting in a more complicated magnetic behavior that is less conducive to strong ferromagnetism **(Ibach&Lüth, 2013; Orbay et al., 2023)**. However, RE-TM HEAs yield large atomic radii difference and negative enthalpy of mixing values. This creates high-entropy bulk metallic glasses (HE-BMGs) and impedes crystallization. There are more studies on magnetocaloric HE-BMGs than RE-HEAs since thermal processing allows for more manipulation of microstructures **(Law & Franco, 2022)**.

As can be observed in Gd-Tb-Dy-Al-M (M = Fe, Co, and Ni), the T_c of $Gd_{20}Tb_{20}Dy_{20}Ni_{20}Al_{20}$, $Gd_{20}Tb_{20}Dy_{20}Co_{20}Al_{20}$, and $Gd_{20}Tb_{20}Dy_{20}Fe_{20}Al_{20}$ are 45 k, 58 k, and 112 k, respectively. According to the author, the reason why T_c is higher with the transition metal Fe than with Ni is because Ni ($3d^8$) has fewer unpaired electrons in 3d than Fe ($3d^6$), which lowers the exchange interaction and, thus, the T_c. On the other hand, the decreases with the Fe rather than Ni due to the antiparallel coupling between the 3d magnetic moment of Fe, Co, and Ni and the 4f moment of Tb, Gd, and Dy; therefore, the total magnetization decreases, and thus the magnetic entropy change **(J. T. Huo et al., 2015).**

Table 4.7 shows the synthesis method, Curie transition (T_C), saturation magnetization, and the maximum change in the magnetic entropy ΔS_m^{peak} of different equiatomic compounds of the HEAs.

Composition	Synthesis Method	ΔS_m^{peak} (J/kgK)	$\mu_0 H$ (T)	T_C (K)	Saturation magnetization (emu/g)	References
FeCoNiCrAl	Arc melting	-	2	277	25	**(Na et al., 2017)**
FeCoNiCr	Arc melting	-	2	104	0.5	**(Na et al., 2017)**
FeCoNiCrGa	Arc melting	-	2	703	38	**(Na et al., 2017)**
FeCoCrNi	Cold rolled	0.35	2	130	-	**(Lucas et al., 2013)**
$Gd_{20}Tb_{20}Dy_{20}Co_{20}Al_{20}$	Arc melting	9.43	5	58	-	**(J. T. Huo et al., 2015)**
$Gd_{20}Tb_{20}Dy_{20}Ni_{20}Al_{20}$	Arc melting	7.25	5	45	-	**(J. T. Huo et al., 2015)**
$Gd_{20}Tb_{20}Dy_{20}Fe_{20}Al_{20}$	Arc melting	5.96	5	112	-	**(J. T. Huo et al., 2015)**

According to table 4.8, without the use of rare earth elements, the composition $(Fe,Mn,Ni)_{66.7}(Ge_{0.45}\ Si_{0.55})_{33.3}$ exhibits the largest isothermal magnetic entropy change $\Delta S_m^{peak} = 13.1 J/kgK$ till 2021, per the study conducted by Law et al. The gap between HEAs and traditional magnetocaloric materials was filled via magneto-structural transformation, which also made it possible to conduct further HEA research **(Law et al., 2021)**.$(MnNi)_{0.6}Si_{0.62}(FeCo)_{0.4}Ge_{0.38}$ show high magnetic entropy change due to the magnetic moment of the Mn and the interaction of the Fe and Mn **(Zheng et al., 2023)**.

In $Al_{50}Cr_{21-x}Mn_{17+x}Co_{12}$ (x = 0, 4, and 8), the alloy exhibits a dual-phase microstructure with

B2 and BCC phases. The B2 phase (a highly ordered intermetallic structure) is responsible for the primary magnetic properties, while the BCC phase has limited magnetization. Increasing Mn content and reducing Cr leads to a higher magnetization and Curie temperature, likely because Mn contributes more effectively to ferromagnetic ordering within the B2 phase. Cr, by contrast, tends to reduce ferromagnetic interactions when it is more abundant. The increase in Mn promotes stronger ferromagnetic exchange interactions in the alloy. In the B2 structure, Mn's magnetic interactions with neighboring atoms, especially with Co and Cr, result in a more robust ferromagnetic alignment compared to Cr-rich compositions. This leads to a stronger overall magnetization and a higher Curie temperature. With the Mn/Cr ratio increasing, the material's magnetic entropy change and adiabatic temperature change also improve, enhancing the alloy's magnetocaloric properties. This improvement is attributed to the larger magnetic moment of Mn, which contributes more significantly to the entropy change during magnetic transitions compared to Cr. Finally, the authors suggest that increasing Mn while reducing Cr contributes to the stability of the B2 phase, which is more favorable for magnetocaloric applications due to its stronger magnetic response. This stable dual-phase microstructure, with Mn-rich B2 regions, enhances the magnetocaloric performance and overall magnetic characteristics of the alloy **(Dastanpour et al., 2024)**.

Table (A-4.8) shows the synthesis method, Curie transition (T_C), the adiabatic temperature changeΔT_{ad}^{peak}, relative cooling power (RCP), and the maximum change in the magnetic entropy ΔS_m^{peak} of different nonequiatomic compounds of the HEAs.

Composition	Synthesis Method	ΔT_{ad}^{peak} (K)	ΔS_m^{peak} (J/kgK)	RCP (JKg^{-1})	$\mu_0 H$ (T)	T_C (K)	References
$Al_{50}Cr_{21}Mn_{17}Co_{12}$	Arc melting	0.071	0.2	-	0.82	287	(Dastanpour et al., 2024)
$Al_{50}Cr_{17}Mn_{21}Co_{12}$	Arc melting	0.102	0.25	16.25	0.82	327	(Dastanpour et al., 2024)

Table (B-4.8) shows the synthesis method, Curie transition (T_C), the adiabatic temperature changeΔT_{ad}^{peak}, relative cooling power (RCP), and the maximum change in the magnetic entropy ΔS_m^{peak} of different nonequiatomic compounds of the HEAs.

$Al_{50}Cr_{13}Mn_{25}Co_{12}$	Arc melting	0.123	0.3	18.9	0.82	339	**(Dastanpour et al., 2024)**
$(Fe,Mn,Ni)_{66.7}(Ge_{0.45}Si_{0.55})_{33.3}$	Arc melting	-	13.1	-	2.5	203	**(Law et al., 2021)**
$(MnNi)_{0.6}Si_{0.62}(FeCo)_{0.4}Ge_{0.38}$	Arc melting	-	48.5	-	5	308.8	**(Zheng et al., 2023)**

Various rare earth magnetocaloric HEAs compositions are depicted in Figure 4.13. They are not suitable for magnetic refrigeration because, as the figure shows, HEAs containing rare earth (RE) elements have strong magnetic entropy changes up to 15.73 J/kgK in TmHoErCoCu and 11.1 J/kgK in GdHoErCoCu. However, their Curie temperatures are significantly lower than room temperature, with the highest value in the figure being 50 K in GdHoCoAl. On the other hand, as seen in figure 4.14, RE-free HEAs have T_C close to room temperature like AlCrFeCoNiCu, but their magnetic entropy change is comparatively small; it didn't exceed 1 J/kgK in the figure.

The lower values of Curie temperature in RE are attributed to the fact that in RE elements, magnetism arises mainly from the 4f electrons, which are shielded by the outer 5s and 5p electron shells. This shielding reduces the direct overlap between magnetic orbitals of neighboring atoms, leading to weaker exchange interactions (the forces that align magnetic moments in a ferromagnetic material) **(J. Lucas et al., 2015)**. In rare earths, the exchange interaction is often mediated by the Ruderman–Kittel–Kasuya–Yosida interaction (RKKY), which itself is weaker than the direct exchange interactions. Spin orbit coupling (SOC) further reduces the exchange strength by modifying the magnetic moment configuration into orbital components, reducing the purely spin-based interaction that drives conventional exchange coupling. SOC introduces magnetic anisotropy; it reduces the flexibility of

moments to align due to exchange interactions; and it also reduces the range of RKKY oscillations **(Huang, 2010)**. In RE-based HEAs, the exchange interactions are generally weaker due to factors like shielding of the 4f electrons, large atomic spacing, and spin-orbit coupling, which all contribute to a low T_c and weaker stability of ferromagnetic order. The large magnetic entropy change values are due to the larger magnetic moments that exist in rare earth elements such as Gadolinium (Gd), Dysprosium (Dy), and Terbium (Tb) due to unpaired 4F electrons in their valency configuration. When an external magnetic field is applied, these large moments align into the field direction more significantly, leading to a more ordered state and finally a larger change in magnetic entropy **(Buschow & de Boer, 2003; Tishin & Spichkin, 2003).** Another reason is due to strong spin-orbit coupling. RE elements famous for this SOC **(L. Zhang et al., 2018)**. In general, SOC causes magnetic anisotropy, which means the magnetic properties of the material depend on the direction of the magnetization resultant direction of the magnetic moments with respect to the crystallographic axes. SOC align election's spin preferentially along a particular direction in these RE-HEAs, leading to a more magnetically ordered state below T_c at low temperature. At T_c, the thermal fluctuations/agitations disrupt these aligned moments in a significant manner; therefore, there is a large difference in the magnetic entropy between the regions below and above T_c. Another important reason is that the lower T_c increases magnetic entropy change. Lower T_c means the magnetic order is easily destroyed by small temperature change at T_c. That means a small temperature change can cause a significant reorientation of magnetic moments, resulting in a higher magnetic entropy change during the magnetic transition. However, strong magnetic interactions in RE-free HEA (transition metals) result in greater T_c. So, they are susceptible to the small temperature changes, but the magnetic order will destroy any way at high temperature regions. Therefore, we can't observe, much change in magnetic entropy in transition metal based alloys **(Buschow & de Boer, 2003; Tishin & Spichkin, 2003).**

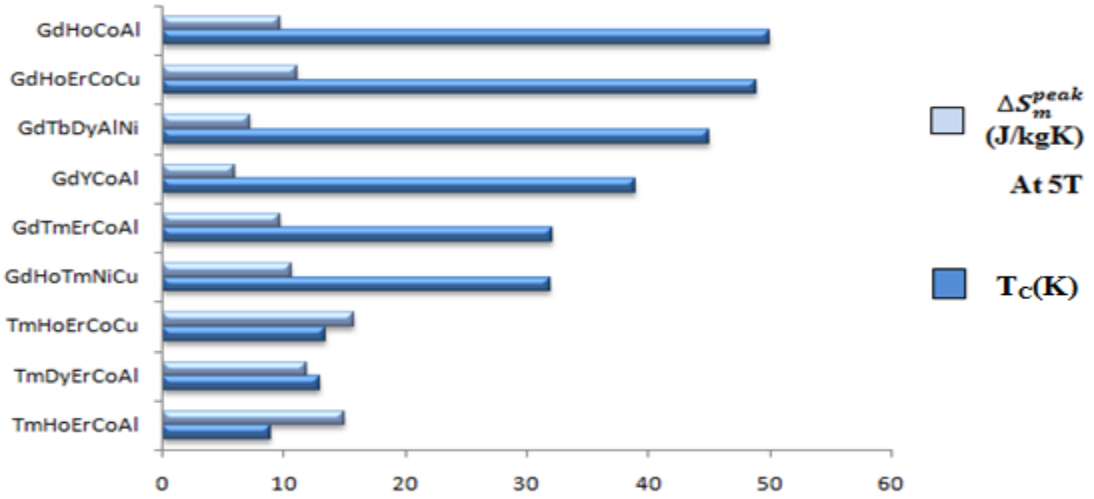

Figure 4.13 The maximum magnetic entropy change ΔS_m^{peak} and the Curie temperature T_C of different compounds of RE- HEAs at 5T **(Cai et al., 2021; Dong et al., 2020; J. Huo et al., 2015; J. T. Huo et al., 2015; J. Li et al., 2018; L. Li et al., 2018; Pang et al., 2020; Xue et al., 2019; Y. Zhang et al., 2021)**.

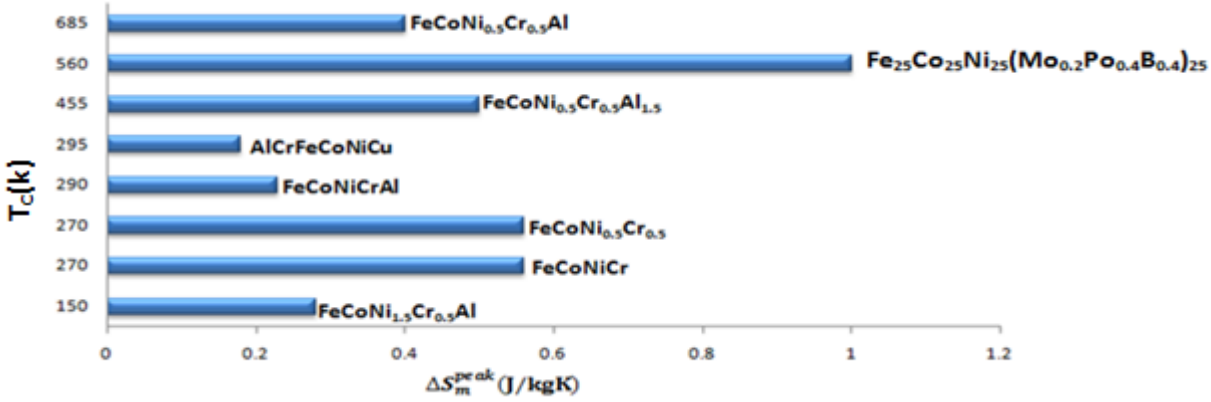

Figure 4.14 The maximum magnetic entropy change ΔS_m^{peak} and the Curie temperature T_C of different compounds of RE- free HEAs at 2 T **(Belyea et al., 2015; Na et al., 2019; Quintana-Nedelcos et al., 2021; Vorobiov et al., 2021; Wu et al., 2019)**.

Chapter 5

Conclusions and Future Work

5.1 Conclusions

In this thesis, a thorough examination of current trends and potential materials for use in magnetic refrigeration is provided, such as $La(Fe,Si)_{13}$, Ni_2–Mn-X-based Heusler alloys (H•A•s) (particularly for X = In, Sn, and Ga), and the HEAs. The Ni-Mn-based Heusler alloys show an abrupt change in the magnetization due to a first-order magnetostructural transition from an austenitic ferromagnetic phase to a low-magnetization martensite phase. In Ni-Mn-Ga alloys, when compared between them according to their physical form, the bulk single crystal shows the high magnetic entropy change due to strong magnetocrystalline anisotropy. The magnetic entropy change of the nanowires and microwires can be enhanced by doping. The martensite transition temperature (T_m) changed by altering the e/a ratio or the cell volume.

The $La(Fe,Si)_{13}$ compounds are the first example of realizing the itinerant-electron metamagnetic transition from the paramagnetic to the ferromagnetic state. In $LaFe_{13-x}Si_x$ alloys, as the Si concentration increases from X = 1.4 to X = 2, the T_c increases due to the change in the electronic structure and the increase in the DOS. The annealing times of the $La(Fe,Si)_{13}$ differ for different synthesis methods. For the arc melting, the cooling rates are slower, leading to larger grain sizes; this typically requires longer annealing times in contrast to ball milling and melt spinning. The MCE and T_c can be adjusted in $La(Fe,Si)_{13}$-based alloys by changing the Fe-Fe interbond distances, magnetic exchange coupling, and lattice parameters by partially substituting La with elements such as Ce and Pr, and by partially

substituting Fe with elements like Ni and C, or by doping with the light elements such as C, H, or a combination of both.

In the high-entropy alloys (HEAs), the base alloy, alloying element additions, resultant phases, and their volume fractions all affect the HEAs' magnetic properties. In the FeCoNiCr-based alloy, by adding Al and Ga, the BCC phase increases the ferromagnetic properties because BCC has a lower coordination number than FCC and a shorter lattice parameter than FCC that facilitates more freedom for magnetic moment alignment, which tends to increase magnetization. FCC has greater lattice parameter, coordination number, and packing fraction than BCC. This close-packed structure introduces more competing magnetic interactions, which can make it harder for magnetic moments to fully align in a ferromagnetic configuration.The RE-HEAs show a small Curie temperature due to the exchange interactions, which are generally weaker due to factors like shielding of the 4F electrons, large atomic spacing, and spin-orbit coupling, which all contribute to a low $T_{c;}$ however, they show a strong magnetic entropy change due to the larger magnetic moments that exist in rare earth elements and the strong spin-orbit coupling, in contrast to the RE-free HEAs (transition metals), which show a greater T_c due to the strong exchange interaction but with a small magnetic entropy change.

5.2 Future Work

Since the bulk properties of those MCE materials ($La(Fe,Si)_{13}$, Ni_2–Mn-X-based Heusler alloys (H•A•s), and the HEAs) were examined in this thesis, the next step would be local probe studies of those materials. To examine structural and magnetic properties in detail, one can use advanced techniques like X-ray absorption spectroscopy, high magnetic field measurements, and neutron scattering because they provide localized information and concentrate on a specific location within the material. For instance, a single magnetic domain or a particle portion of the material can be selected. In contrast, bulk studies like magnetization measurements (M vs. T, M vs. H) and specific heat measurements provide an average value of all the localized responses. By combining these complementary approaches,

a more comprehensive understanding of magnetocaloric materials can be achieved, leading to the development of even more efficient and innovative devices.

References

Abboushi, N. (2021). *Macroscopic magnetic properties and magnetocaloric effect in single crystalline Mn_5Si_3 and derived compounds* [Master's thesis, Al Quds University]. https://juser.fz-juelich.de/record/892880/export/he?ln=en

Ahn, K. (2024). Ni-Mn based conventional full Heusler alloys, all-d-metal full Heusler alloys, and their promising functional properties to solid state cooling by magnetocaloric effect. *Journal of Alloys and Compounds*, *978*, 173378. https://doi.org/10.1016/j.jallcom.2023.173378

Ali, A., Chiang, Y. W., & Santos, R. M. (2022). X-ray Diffraction Techniques for Mineral Characterization: A Review for Engineers of the Fundamentals, Applications, and Research Directions. *Minerals*, *12*(2), Article 2. https://doi.org/10.3390/min12020205

Aliev, A. M., Gamzatov, A. G., Batdalov, A. B., Kalitka, V. S., & Kaul, A. R. (2011). Direct and Inverse Magnetocaloric effects in A-site ordered $PrBaMn_2O_6$ manganite in low magnetic fields. *Journal of Alloys and Compounds*, *509*(17), L165–L167. https://doi.org/10.1016/j.jallcom.2011.02.058

Al-Namourah, K. K. J. (2019). *Synthesis , magnetic properties and crystal structures of magnetocaloric materials in the system (Mn_5Ge_3)*. [Master's thesis, Al Quds University] https://www.semanticscholar.org/paper/Synthesis-%2C-magnetic-properties-and-crystal-of-in-(-Al-Namourah/94a21437a193c1265788b7625b1ff8e0f018f2f4

Al-Shataif, Y., S., S., Al-Mufadi, F., Alaboodi, A., & Ammar, H. (2019). Manufacturing Methods, Microstructural and Mechanical Properties Evolutions of High-Entropy Alloys: A Review. *Metals and Materials International*, *26*, 3. https://doi.org/10.1007/s12540-019-00565-z

Al-Zubi, A. (2010). *Ab initio investigations of magnetic properties of ultrathin transition-metal films on 4d substrates*.

Anderson, W. (1984). *Basic Notions Of Condensed Matter Physics*. Basic Books.

Asli, N., Dahmane, F., Mokhtari, M., Zouaneb, C., Mohammed, B. M., Khachai, H., Srivastava, V., Naqib, S., Al-Douri, Y., Bouhemadou, A., &Khenata, R. (2021). Structural, electronic, magnetic and mechanical properties of the full-Heusler compounds $Ni_2Mn(Ge,Sn)$ and Mn_2NiGe. *ZeitschriftFürNaturforschung A*, *76*. https://doi.org/10.1515/zna-2020-0329

Basso, V. (2017). *Basics of the magnetocaloric effect* (arXiv:1702.08347). arXiv. http://arxiv.org/abs/1702.08347

Belyea, D., Lucas, M., Michel, E., Horwath, J., & Miller, C. (2015). Tunable magnetocaloric effect in transition metal alloys. *Scientific Reports*, *5*, 15755. https://doi.org/10.1038/srep15755

Benka, G. (2021). *Preparation and Investigation of Intermetallic Magnetic Compounds with Disorder*.

Bhatt, K., Singh, N., & Singh, H. (2024). *Structural And Magnetic Properties of Ni_2-xCoxMnSn (x=0,1) Based Heusler Alloy.*https://doi.org/10.1063/5.0178035

Biniskos, N. (2018). *Inelastic neutron scattering on magnetocaloric compounds* [CEA]. https://www.mem-lab.fr/en/Pages/MDN/Theses/Nikolaos-Biniskos.aspx

Brown, G. V. (1976). Magnetic heat pumping near room temperature. *Journal of Applied Physics*, *47*(8), 3673–3680. https://doi.org/10.1063/1.323176

Buschow, K. H. J., & de Boer, F. R. (2003). Introduction. In K. H. J. Buschow& F. R. de Boer (Eds.), *Physics of Magnetism and Magnetic Materials* (pp. 1–2). Springer US. https://doi.org/10.1007/0-306-48408-0_1

Cai, M., Luo, Q., Zeng, Q., & Shen, B. (2021). Combined effect of demagnetization field and magnetic anisotropy on magnetocaloric behavior and magnetocaloric-magnetoresistance correlation in GdTmErCoAl high-entropy amorphous alloy. *Journal of Magnetism and Magnetic Materials*, *528*, 167817. https://doi.org/10.1016/j.jmmm.2021.167817

Cantor, B., Chang, I. T. H., Knight, P., & Vincent, A. J. B. (2004). Microstructural development in equiatomic multicomponent alloys. *Materials Science and Engineering: A*, *375–377*, 213–218. https://doi.org/10.1016/j.msea.2003.10.257

Casanova iFernàndez, F. (2004). *Magnetocaloric Effect In $Gd_5(Si_xGe_{1-x})_4$ Alloys*. [Doctoralsdissertion, Universitat de Barcelona]. https://diposit.ub.edu/dspace/handle/2445/41817

Chaudhary, V., Chaudhary, R., Banerjee, R., & Ramanujan, R. V. (2021). Accelerated and conventional development of magnetic high entropy alloys. *Materials Today*, *49*, 231–252. https://doi.org/10.1016/j.mattod.2021.03.018

Cicek, M. M., Saritas, S., Yildirim, O., & Emre, B. (2020). Effect of the low constituent boron on martensitic transformation, magnetic, and magnetocaloric properties of $Ni_{50}Mn_{35}In_{15}$ Heusler alloys. *Journal of Alloys and Compounds*, *845*, 155493. https://doi.org/10.1016/j.jallcom.2020.155493

Cipelletti, L., Trappe, V., & Pine, D. J. (2016). Scattering Techniques. In *Fluids, Colloids and Soft Materials* (pp. 131–148). John Wiley & Sons, Ltd. https://doi.org/10.1002/9781119220510.ch8

Clearfield, A., &Bhuvanesh, N. (2008). X-Ray Powder Diffraction. In *Encyclopedia of Inorganic Chemistry*. John Wiley & Sons, Ltd. https://doi.org/10.1002/0470862106.ia332

Coey, J. M. D., &Mazaleyrat, F. (2023). History of magnetism. In *Encyclopedia of Condensed Matter Physics* (pp. 1–17). Elsevier. https://doi.org/10.1016/B978-0-323-90800-9.00155-4

Cullity, B. D., & Graham, C. D. (2011). *Introduction to Magnetic Materials*. John Wiley & Sons.

Dan, N., Duc, N., Nguyen, H., Thanh, P., Bau, L., An, N., Anh, D., Bang, N., Mai, N., Anh, P., Thanh, T., Phan, T., & Yu, S. C. (2014). Magnetic properties and magnetocaloric effect in Ni-Mn-Sn alloys. *Journal of Magnetism and Magnetic Materials*, *374*. https://doi.org/10.1016/j.jmmm.2014.08.061

Dastanpour, E., Huang, S., Ström, V., Varga, L. K., Vitos, L., &Schönecker, S. (2024). *An assessment of the* $Al_{50}Cr_{21-x}Mn_{17+x}Co_{12}$ (x=0, 4, 8) high-entropy alloys for magnetocaloric refrigeration application. *Journal of Alloys and Compounds*, *984*, 173977. https://doi.org/10.1016/j.jallcom.2024.173977

Design, Q. (2011). Vibrating Sample Magnetometer (VSM) Option User's Manual. no, 1096, 122.

Dong, Z., Wang, Z., & Yin, S. (2020). Magnetic properties and large cryogenic magneto-caloric effect of $Er_{0.2}Tm_{0.2}Ho_{0.2}Cu_{0.2}Co_{0.2}$ amorphous ribbon. *Intermetallics*, *124*, 106879. https://doi.org/10.1016/j.intermet.2020.106879

Drenth, J. (1994). Laue Diffraction. In J. Drenth (Ed.), *Principles of Protein X-ray Crystallography* (pp. 234–241). Springer. https://doi.org/10.1007/978-1-4757-2335-9_12

Eggert, B. G. F., Belo, J. F. H., Araújo, J. P., Hauback, B. C., &Frommen, C. (2023). Structural transitions and magnetocaloric properties of low-cost MnNiSi-based intermetallics. *Intermetallics*, *154*, 107823. https://doi.org/10.1016/j.intermet.2023.107823

Engdahl, G. (2021). *Handbook Of Electrical Steel*. World Scientific.

Fatimah, S., Ragadhita, R., Al Husaeni, D. F., &Nandiyanto, A. (2021). How to Calculate Crystallite Size from X-Ray Diffraction (XRD) using Scherrer Method. *ASEAN Journal of Science and Engineering*, *2*, 65–76. https://doi.org/10.17509/ajse.v2i1.37647

Foadian, F., Kremer, R., &Khani, S. (2023). Chapter Fourteen—Rapid alloying in additive manufacturing using integrated computational materials engineering. In J. Kadkhodapour, S. Schmauder, & F. Sajadi (Eds.), *Quality Analysis of Additively Manufactured Metals* (pp. 583–624). Elsevier. https://doi.org/10.1016/B978-0-323-88664-2.00007-5

Franco, V., Blázquez, J. S., Ingale, B., & Conde, A. (2012). The Magnetocaloric Effect and Magnetic Refrigeration Near Room Temperature: Materials and Models. *Annual Review of Materials Research*, *42*(Volume 42, 2012), 305–342. https://doi.org/10.1146/annurev-matsci-062910-100356

Fujita, A., Fujieda, S., Hasegawa, Y., &Fukamichi, K. (2003). Itinerant-electron metamagnetic transition and large magnetocaloric effects in $La(Fe_xSi_{1-x})_{13}$ compounds and their hydrides. *Physical Review B*, *67*(10), 104416. https://doi.org/10.1103/PhysRevB.67.104416

Fujita, A., Fukamichi, K., Wang, J.-T., & Kawazoe, Y. (2003). Large magnetovolume effects and band structure of itinerant-electron metamagnetic $La(Fe_xSi_{1-x})_{13}$ compounds. *Physical Review B*, *68*(10), 104431. https://doi.org/10.1103/PhysRevB.68.104431

Gabbott, P. (2008). *Principles and Applications of Thermal Analysis*. John Wiley & Sons.

Gerin, M. (2022). *Synthesis, high pressure behaviour and metastable phases of Si_xGe_{1-x} alloys*.

Ghahremani, M. (2014). *Magnetocaloric Materials and Magnetic Refrigeration Systems*.

Ghorai, S. (2022). *Direct and indirect magnetocaloric properties of first- and second-order phase transition materials*.

Ghorbani-Zavareh, M. (2016). *Direct Measurements of the Magnetocaloric Effect in Pulsed Magnetic Fields*.Germany: Technische Universität Dresden.

Glavatskyy, I., Glavatska, N., Dobrinsky, A., Hoffmann, J.-U., Söderberg, O., & Hannula, S.-P. (2007). Crystal structure and high-temperature magnetoplasticity in the new Ni–Mn–Ga–Cu magnetic shape memory alloys. *ScriptaMaterialia*, *56*(7), 565–568. https://doi.org/10.1016/j.scriptamat.2006.12.019

Gottschall, T., Skokov, K. P., Fries, M., Taubel, A., Radulov, I., Scheibel, F., Benke, D., Riegg, S., &Gutfleisch, O. (2019). Making a Cool Choice: The Materials Library of Magnetic Refrigeration. *Advanced Energy Materials*, *9*(34), 1901322. https://doi.org/10.1002/aenm.201901322

Gottschall, T. (2016). *On the Magnetocaloric Properties of Heusler Compounds: Reversible,*

Guo, W., Dmowski, W., Noh, J.-Y., Rack, P., Liaw, P., & Egami, T. (2012). Local Atomic Structure of a High-Entropy Alloy: An X-Ray and Neutron Scattering Study. *Metallurgical and Materials Transactions A*, *44*. https://doi.org/10.1007/s11661-012-1474-0

Gutfleisch, O., Yan, A., & Müller, K.-H. (2005). Large magnetocaloric effect in melt-spun LaFe13−xSix. *Journal of Applied Physics*, *97*(10), 10M305. https://doi.org/10.1063/1.1847871

Hou, X., Lampen-Kelley, P., Xue, Y., Liu, C., Xu, H., Han, N., Ma, C., Srikanth, H., & Phan, M.-H. (2015). Formation mechanisms of NaZn13-type phase in giant magnetocaloric La–Fe–Si compounds during rapid solidification and annealing. *Journal of Alloys and Compounds*, *646*, 503–511. https://doi.org/10.1016/j.jallcom.2015.05.173

Hu, F., Ilyn, M., Tishin, A., Sun, J., Wang, G., Chen, Y.-F., Wang, F., Cheng, Z.-H., & Shen, B. (2003). Direct measurements of magnetocaloric effect in the first-order system $LaFe_{11.7}Si_{1.3}$. *Journal of Applied Physics*, *93*, 5503–5506. https://doi.org/10.1063/1.1563036

Huang, C.-H. (2010). *Rare Earth Coordination Chemistry: Fundamentals and Applications*. John Wiley & Sons.

Huo, J. T., Huo, L., Men, H., Wang, X., Inoue, A., Wang, J., Chang, C., & Li, R.-W. (2015). The magnetocaloric effect of Gd-Tb-Dy-Al-M (M = Fe, Co and Ni) high-entropy bulk metallic glasses. *Intermetallics*, *58*, 31–35. https://doi.org/10.1016/j.intermet.2014.11.004

Huo, J., Huo, L., Li, J., Men, H., Wang, X., Inoue, A., Chang, C., Wang, J.-Q., & Li, R.-W. (2015). High-entropy bulk metallic glasses as promising magnetic refrigerants. *Journal of Applied Physics*, *117*(7), 073902. https://doi.org/10.1063/1.4908286

Ibach, H., &Lüth, H. (2013). *Solid-State Physics: An Introduction to Principles of Materials Science*. Springer Science & Business Media.

Ipus, J. J., Borrego, J. M., Moreno-Ramírez, L. M., Blázquez, J. S., Franco, V., & Conde, A. (2017). Grinding and particle size selection as a procedure to enhance the magnetocaloric response of La(Fe,Si)13 bulk samples. *Intermetallics*, *84*, 30–34. https://doi.org/10.1016/j.intermet.2016.12.022

Iwashita, N. (2016). Chapter 2—X-ray Powder Diffraction. In M. Inagaki & F. Kang (Eds.), *Materials Science and Engineering of Carbon* (pp. 7–25). Butterworth-Heinemann. https://doi.org/10.1016/B978-0-12-805256-3.00002-7

Jakubovics, J. P. (2023). *Magnetism and Magnetic Materials* (2nd ed.). CRC Press. https://doi.org/10.1201/9781003422044

Jendrzejewska, I. (2020). Application of X-Ray Powder Diffraction for Analysis of Selected Dietary Supplements Containing Magnesium and Calcium. *Frontiers in Chemistry*, *8*, 672. https://doi.org/10.3389/fchem.2020.00672

Jendrzejewska, I., Musiol, R., Goryczka, T., Pietrasik, E., Klimontko, J., &Jampilek, J. (2021). The Usefulness of X-ray Diffraction and Thermal Analysis to Study Dietary Supplements Containing Iron. *Molecules*, *27*, 197. https://doi.org/10.3390/molecules27010197

Jeppesen, S., Linderoth, S., Pryds, N., Kuhn, L., & Jensen, J. (2008). Indirect Measurement of the Magnetocaloric Effect Using a Novel Differential Scanning Calorimeter with Magnetic Field. *The Review of Scientific Instruments*, *79*, 083901. https://doi.org/10.1063/1.2957611

Kadiyala, C. B. N., .N, R., Prakash, M., Uppara, N., Nagasamudram, S. K., Sarmash, S., Subbarao, T., Kumar, R., & Kumar, G. (2018). Review on Magnetocaloric Effect and Materials. *Journal of Superconductivity and Novel Magnetism*, *31*. https://doi.org/10.1007/s10948-018-4666-z

Kamantsev, A. P., Koshkid'ko, Y. S., Gaifullin, R. Y., Musabirov, I. I., Koshelev, A. V., Mashirov, A. V., Sokolovskiy, V. V., Buchelnikov, V. D., Ćwik, J., &Shavrov, V. G. (2023). Inverse Magnetocaloric Effect in Heusler $Ni_{44.4}Mn_{36.2}Sn_{14.9}Cu_{4.5}$ Alloy at Low Temperatures. *Metals*, *13*(12), Article 12. https://doi.org/10.3390/met13121985

Kavita, S., Ramakrishna, V. V., Yadav, P., Kethavath, S., Lalla, N. P., Thomas, T., Bhatt, P., & Gopalan, R. (2019). Enhancement of martensite transition temperature and inverse magnetocaloric effect in Ni43Mn47Sn11 alloy with B doping. *Journal of Alloys and Compounds*, *795*, 519–527. https://doi.org/10.1016/j.jallcom.2019.04.269

Ke, Y.-J., Zhang, X.-Q., Ma, Y., & Cheng, Z.-H. (2016). Anisotropic magnetic entropy change in RFeO3 single crystals(R = Tb, Tm, or Y). *Scientific Reports*, *6*(1), 19775. https://doi.org/10.1038/srep19775

Khan, M. (2007). Magnetic entropy changes and exchange bias effects associated with phase transitions in ferromagnetic Heusler alloys. In *Ph.D. Thesis*. https://ui.adsabs.harvard.edu/abs/2007PhDT.....203K

Khovailo, V. V., Chernenko, V. A., Cherechukin, A. A., Takagi, T., & Abe, T. (2004). An efficient control of Curie temperature *T*C in Ni–Mn–Ga alloys. *Journal of Magnetism and Magnetic Materials*, *272–276*, 2067–2068. https://doi.org/10.1016/j.jmmm.2003.12.836

Kitanovski, A. (2020). Energy Applications of Magnetocaloric Materials. *Advanced Energy Materials*, *10*(10), 1903741. https://doi.org/10.1002/aenm.201903741

Kittel, C. (2005). *Introduction to solid state physics* (8th ed). Wiley.

Klems, B. A. (2002). *Magnetic refrigerator developed by Ames*. 24.

Koblischka, M., &Koblischka-Veneva, A. (2022). Superconductivity 2022. *Metals*, *12*, 568. https://doi.org/10.3390/met12040568

Kulkova, S. E., Eremeev, S. V., Kakeshita, T., Kulkov, S. S., &Rudenski, G. E. (2006). The Electronic Structure and Magnetic Properties of Full- and Half-Heusler Alloys. *MATERIALS TRANSACTIONS*, *47*(3), 599–606. https://doi.org/10.2320/matertrans.47.599

Kumar, N. P., Singh, M., Mahey, V., Nautiyal, S., Kumar, D. M. R., Rao, N. V. R., & Raja, M. M. (2020). Effect of Si substitution on the Structural, Magnetic and Magnetocaloric Properties of Ni–Mn–In Heusler alloys. *Applied Physics A*, *126*(6), 472. https://doi.org/10.1007/s00339-020-03651-x

Kusama, T., Omori, T., Saito, T., Kise, S., Tanaka, T., Araki, Y., &Kainuma, R. (2017). Ultra-large single crystals by abnormal grain growth. *Nature Communications*, *8*, 1–9. https://doi.org/10.1038/s41467-017-00383-0

Ladd, M., & Palmer, R. (2013). *Structure Determination by X-ray Crystallography: Analysis by X-rays and Neutrons*. Springer US. https://doi.org/10.1007/978-1-4614-3954-7

Lamas, D. G., de Oliveira Neto, M., Kellermann, G., &Craievich, A. F. (2017). 5—X-Ray Diffraction and Scattering by Nanomaterials. In A. L. Da Róz, M. Ferreira, F. de Lima Leite, & O. N. Oliveira (Eds.), *Nanocharacterization Techniques* (pp. 111–182). William Andrew Publishing. https://doi.org/10.1016/B978-0-323-49778-7.00005-9

Law, J. Y., & Franco, V. (2022). Review on magnetocaloric high-entropy alloys: Design and analysis methods. *Journal of Materials Research*, *38*(1), 37–51. https://doi.org/10.1557/s43578-022-00712-0

Law, J. Y., Díaz-García, Á., Moreno-Ramírez, L. M., & Franco, V. (2021). Increased magnetocaloric response of FeMnNiGeSi high-entropy alloys. *Acta Materialia*, *212*, 116931. https://doi.org/10.1016/j.actamat.2021.116931

Law, J. Y., Moreno-Ramírez, L. M., Díaz-García, Á., & Franco, V. (2023). Current perspective in magnetocaloric materials research. *Journal of Applied Physics*, *133*(4), 040903. https://doi.org/10.1063/5.0130035

Lee, M. (2016). Laue Method and Determination of Single Crystal Orientation. In *X-Ray Diffraction for Materials Research*. Apple Academic Press.

Li, J., Xue, L., Yang, W., Yuan, C., Huo, J., & Shen, B. (2018). Distinct spin glass behavior and excellent magnetocaloric effect in $Er_{20}Dy_{20}Co_{20}Al_{20}RE_{20}$ (RE = Gd, Tb and Tm) high-entropy bulk metallic glasses. *Intermetallics*, *96*, 90–93. https://doi.org/10.1016/j.intermet.2018.03.002

Li, L., Xu, C., Yuan, Y., & Zhou, S. (2018). Large refrigerant capacity induced by table-like magnetocaloric effect in amorphous $Er_{0.2}Gd_{0.2}Ho_{0.2}Co_{0.2}Cu_{0.2}$ ribbons. *Materials Research Letters*. https://www.tandfonline.com/doi/abs/10.1080/21663831.2018.1471749

Li, L.-W. (2016). Review of magnetic properties and magnetocaloric effect in the intermetallic compounds of rare earth with low boiling point metals. *Chinese Physics B*, *25*(3), 037502. https://doi.org/10.1088/1674-1056/25/3/037502

Li, Z., Zhang, Y., Sánchez-Valdés, C. F., Sánchez Llamazares, J. L., Esling, C., Zhao, X., &Zuo, L. (2014). Giant magnetocaloric effect in melt-spun Ni-Mn-Ga ribbons with magneto-multistructural transformation. *Applied Physics Letters*, *104*(4), 044101. https://doi.org/10.1063/1.4863273

Lionte, D. (2015). *Characterization, study and modelling of the thermomagnetic behaviour of a magnetic refrigeration system with nonlinear materials and Curie point near room temperature*.

Liu, T., Chen, Y., Tang, Y., Xiao, S., Zhang, E., & Wang, J. (2009). Structure and magnetic properties of shortly high temperature annealing $LaFe_{11.6}Si_{1.4}$ compound. *Journal of Alloys and Compounds*, *475*(1), 672–675. https://doi.org/10.1016/j.jallcom.2008.07.139

Long, F., Song, Y., & Chen, J. (2024). $La(Fe,Si/Al)_{13}$-based materials with exceptional magnetic functionalities: A review. *Microstructures*, *4*(1). https://doi.org/10.20517/microstructures.2023.58

Lucas, J., Lucas, P., Mercier, T., Rollat, A., & Davenport, W. (2015). *Chapter 8. Rare Earth Electronic Structures and Trends in Properties* (pp. 123–139). https://doi.org/10.1016/B978-0-444-62735-3.00008-5

Lucas, M., Belyea, D., Bauer, C., Bryant, N., Michel, E., Turgut, Z., Leontsev, S., Horwath, J., Semiatin, S., & Miller, C. (2013). Thermomagnetic analysis of FeCoCrxNi alloys: Magnetic entropy of high-entropy alloys. *Journal of Applied Physics*, *113*. https://doi.org/10.1063/1.4798340

Lyubina, J. (2017). Magnetocaloric materials for energy efficient cooling. *Journal of Physics D: Applied Physics*, *50*(5), 053002. https://doi.org/10.1088/1361-6463/50/5/053002

Maraytta, N. A. (2021). *Structure and dynamics of magnetocaloric materials* [Online]. RWTH Aachen University.

Mařík, O., &Šimeček, I. (2015). *Acceleration of Le Bail fitting method on parallel platforms*. 136–141.

Md Din, M. F., Wang, J. L., Zeng, R., Shamba, P., Debnath, J. C., & Dou, S. X. (2013). Effects of Cu substitution on structural and magnetic properties of $La_{0.7}Pr_{0.3}Fe_{11.4}Si_{1.6}$ compounds. *Intermetallics*, *36*, 1–7. https://doi.org/10.1016/j.intermet.2012.12.013

Mellari, S. (2023). Introduction to magnetic refrigeration: Magnetocaloric materials. *International Journal of Air-Conditioning and Refrigeration*, *31*(1), 5. https://doi.org/10.1007/s44189-023-00021-z

Mezaal, N. A., Osintsev, K. V., &Zhirgalova, T. B. (2017). Review of magnetic refrigeration system as alternative to conventional refrigeration system. *IOP Conference Series: Earth and Environmental Science*, *87*(3), 032024. https://doi.org/10.1088/1755-1315/87/3/032024

Morrison, K., Betouras, J. J., Venkat, G., Ewings, R. A., Caruana, A. J., Skokov, K. P., Gutfleisch, O., & Cohen, L. F. (2024). Emergence of a Hidden Magnetic Phase in $LaFe_{11.8}Si_{1.2}$ Investigated by Inelastic Neutron Scattering as a Function of Magnetic Field and Temperature. *Advanced Physics Research*, *3*(7), 2400008. https://doi.org/10.1002/apxr.202400008

Moskowitz, L. R. (1995). *Permanent Magnet Design and Application Handbook*. Krieger.

Mozharivskyj, Y. (2023)—Preparation of magnetocaloric materials. In J. Reedijk& K. R. Poeppelmeier (Eds.), *Comprehensive Inorganic Chemistry III (Third Edition)* (pp. 178–198). Elsevier. https://doi.org/10.1016/B978-0-12-823144-9.00077-7

Na, S.-M., Lambert, P., Kim, H., Paglione, J., & Jones, N. (2019). Thermomagnetic properties and magnetocaloric effect of FeCoNiCrAl-type high-entropy alloys. *AIP Advances*, *9*, 035010. https://doi.org/10.1063/1.5079394

Na, S.-M., Yoo, J.-H., Lambert, P. K., & Jones, N. J. (2017). Room-temperature ferromagnetic transitions and the temperature dependence of magnetic behaviors in FeCoNiCr-based high-entropy alloys. *AIP Advances*, *8*(5), 056412. https://doi.org/10.1063/1.5007073

Nazzal, S. N. N. (2023). *Macroscopic magnetic characterization of* ***Mn4FeSi3*** *single crystal* [AL-Quds University]. https://dspace.alquds.edu/handle/20.500.12213/8367

Oke, W., Aldhafferi, N., Saliu, S., Owolabi, T., Alqahtani, A., Almurayh, A., &Qahtan, T. (2023). Modeling the magnetocaloric effect of spinel ferrites for magnetic refrigeration technology using extreme learning machine and genetically hybridized support vector regression computational methods. *Cogent Engineering*, *10*. https://doi.org/10.1080/23311916.2023.2257955

Orbay, Y., Rao, Z., Çakır, A., Tavşanoğlu, T., Farle, M., &Acet, M. (2023). Magnetic properties of the FCC and BCC phases of $(MnFeCoNi)_{80}Cu_{20-x}Z_x$(Z=Al, Ga) high-entropy alloys. *Acta Materialia*, *259*, 119240. https://doi.org/10.1016/j.actamat.2023.119240

Pál, L. (1969). *First-order magnetic phase transitions*.

Pandey, S., Quetz, A., Aryal, A., Dubenko, I., Mazumdar, D., Stadler, S., & Ali, N. (2017). Magnetocaloric, thermal, and magnetotransport properties of $Ni_{50}Mn_{35}In_{13.9}B_{1.1}$ Heusler alloy. *Journal of Magnetism and Magnetic Materials*, *444*, 98–101. https://doi.org/10.1016/j.jmmm.2017.08.009

Pang, C. M., Chen, L., Xu, H., Guo, W., Lv, Z. W., Huo, J. T., Cai, M. J., Shen, B. L., Wang, X. L., & Yuan, C. C. (2020). Effect of Dy, Ho, and Er substitution on the magnetocaloric properties of Gd-Co-Al-Y high entropy bulk metallic glasses. *Journal of Alloys and Compounds*, *827*, 154101. https://doi.org/10.1016/j.jallcom.2020.154101

Panwar, N. (2018). *Magnetism and Magnetic Materials*. BoD – Books on Demand.

Pasquale, M., Sasso, C. P., Lewis, L. H., Giudici, L., Lograsso, T., &Schlagel, D. (2005). Magnetostructural transition and magnetocaloric effect in Ni55Mn20Ga25 single crystals. *Physical Review B*, *72*(9), 094435. https://doi.org/10.1103/PhysRevB.72.094435

Paul-Boncour, V., &Bessais, L. (2021). Tuning the Magnetocaloric Properties of the La(Fe,Si)13 Compounds by Chemical Substitution and Light Element Insertion. *Magnetochemistry*, *7*, 13. https://doi.org/10.3390/magnetochemistry7010013

Pauling, L. (1953). A Theory of Ferromagnetism. *Proceedings of the National Academy of Sciences*, *39*(6), 551–560. https://doi.org/10.1073/pnas.39.6.551

Pecharsky, V. K., &Gschneidner, Jr., K. A. (1997). Giant Magnetocaloric Effect in $Gd_5(Si_2 Ge_2)$. *Physical Review Letters*, *78*(23), 4494–4497. https://doi.org/10.1103/PhysRevLett.78.4494

Pecharsky, V. K., &Gschneidner, K. A. (2005). Magnetocaloric Effect. In F. Bassani, G. L. Liedl, & P. Wyder (Eds.), *Encyclopedia of Condensed Matter Physics* (pp. 236–244). Elsevier. https://doi.org/10.1016/B0-12-369401-9/01127-X

Pecharsky, V., Gschneidner, J., Pecharsky, A., &Tishin, A. (2001). Thermodynamics of the magnetocaloric effect. *Phys. Rev. B*, *64*. https://doi.org/10.1103/PhysRevB.64.144406

Peng, D. R., Zhong, X. C., Dong, X. T., Huang, J. H., Zhang, H., Ma, L., Wu, S. M., Jiao, D. L., Liu, Z. W., Yu, H. Y., Zhang, H., Qiu, W. Q., & Ramanujan, R. V. (2020). Microstructure, phase evolution and magnetocaloric properties of $LaFe_{11.6}Si_{1.4}/La_7Co_3$ composite. *Journal of Alloys and Compounds*, *823*, 153726. https://doi.org/10.1016/j.jallcom.2020.153726

Phan, M.-H., & Yu, S.-C. (2007). Review of the magnetocaloric effect in manganite materials. *Journal of Magnetism and Magnetic Materials*, *308*(2), 325–340. https://doi.org/10.1016/j.jmmm.2006.07.025

Phejar, M., Paul-Boncour, V., &Bessais, L. (2011). Magnetocaloric Study of Mechanically Alloyed LaFeSi. In *TMS Annual Meeting* (Vol. 1, p. 324). https://doi.org/10.1002/9781118062111.ch34

Quantum design, physical property measurement system, heat capacity option user's manual, 19th edition, Quantum Design, San Diego (USA), 2010.

Quintana-Nedelcos, A., Leong, Z., & Morley, N. A. (2021). Study of dual-phase functionalisation of NiCoFeCr-Alx multicomponent alloys for the enhancement of magnetic properties and magneto-caloric effect. *Materials Today Energy*, *20*, 100621. https://doi.org/10.1016/j.mtener.2020.100621

Radelytskyi, I., Pękała, M., Szymczak, R., Gawryluk, D., Berkowski, M., Fink-Finowicki, J., Diduszko, R., Dyakonov, V., &Szymczak, H. (2017). Magnetocaloric effect in Ni_2MnGa single crystal in the vicinity of the martensitic phase transition. *Journal of Magnetism and Magnetic Materials*, *430*. https://doi.org/10.1016/j.jmmm.2017.01.024

Ranke, P. J. von, Oliveira, N. A. de, Alho, B. P., Plaza, E. J. R., Sousa, V. S. R. de, Caron, L., & Reis, M. S. (2009). Understanding the inverse magnetocaloric effect in antiferro- and ferrimagnetic arrangements. *Journal of Physics: Condensed Matter*, *21*(5), 056004. https://doi.org/10.1088/0953-8984/21/5/056004

Río-López, N. A., Lázpita, P., Salazar, D., Petrenko, V. I., Plazaola, F., Chernenko, V., &Porro, J. M. (2021). Neutron Scattering as a Powerful Tool to Investigate Magnetic Shape Memory Alloys: A Review. *Metals*, *11*(5), Article 5. https://doi.org/10.3390/met11050829

Robotti, N. (2013). The discovery of X-ray diffraction. *RendicontiLincei*, *24*(1), 7–18. https://doi.org/10.1007/s12210-012-0205-1

Rosca, M., Balli, M., Fruchart, D., Gignoux, D., Hlil, E. K., Miraglia, S., Ouladdiaf, B., & Wolfers, P. (2010). Neutron diffraction study of $LaFe_{11.31}$ $Si_{1.69}$ and $LaFe_{11.31}Si_{1.69}H_{1.45}$ compounds. *Journal of Alloys and Compounds*, *490*(1), 50–55. https://doi.org/10.1016/j.jallcom.2009.10.093

S, S., K, A., U d, R., S r, A., Dzubinska, A., Reiffers, M., & R, N. (2023). $Ni_{48}Ag_2Mn_{37}In_{13}$ multifunctional alloy: A room temperature inverse magnetocaloric and magnetoresistive material. *Journal of Alloys and Compounds*, *938*, 168590. https://doi.org/10.1016/j.jallcom.2022.168590

Saritaş, S., Çiçek, M. M., Kavak, E., Gurpinar, K., Yildirim, O., Yuce, S., Atakol, O., & Emre, B. (2023). Tuning of the magneto-caloric effects in $Ni_{43}Mn_{46}In_{11}$ magnetic shape memory alloys

by substitution of boron. *Journal of Physics: Condensed Matter*, *36*(7), 075801. https://doi.org/10.1088/1361-648X/ad0a13

Schmid, I. (2008). *The role of uncompensated spins in exchange biased systems*. https://doi.org/10.5451/UNIBAS-004458737

Schmool, D. S., &Markó, D. (2018). Magnetism in Solids: Hysteresis. In *Reference Module in Materials Science and Materials Engineering*. Elsevier. https://doi.org/10.1016/B978-0-12-803581-8.11413-4

Sharma, V. K., Chattopadhyay, M. K., Kumar, R., Ganguli, T., Tiwari, P., & Roy, S. B. (2007). Magnetocaloric effect in Heusler alloys $Ni_{50}Mn_{34}In_{16}$ and $Ni_{50}Mn_{34}Sn_{16}$. *Journal of Physics: Condensed Matter*, *19*(49), 496207. https://doi.org/10.1088/0953-8984/19/49/496207

Shen, B. G., Sun, J. R., Hu, F. X., Zhang, H. W., & Cheng, Z. H. (2009). Recent Progress in Exploring Magnetocaloric Materials. *Advanced Materials*, *21*(45), 4545–4564. https://doi.org/10.1002/adma.200901072

Singh, K. (2023). *Science Laws and Their Applications*. Cambridge Scholars Publishing.

Sivia, D. S. (2011). *Elementary scattering theory: For X-ray and neutron users*. Oxford University Press.

Sochi, T. (2010). *High Throughput Software for Powder Diffraction and its Application to Heterogeneous Catalysis*.

Song, B.-Y., Han, Y.-Q., Cheng, J., Gao, L., Jin, X., Sun, Z.-B., & Huang, J.-H. (2024). Effect of Al doping on magnetocaloric effect and mechanical properties of La(FeSi)13-based alloys. *Journal of Alloys and Compounds*, *990*, 174398. https://doi.org/10.1016/j.jallcom.2024.174398

Sutrisno, H., Ariswan, A., &Purwaningsih, D. (2018). Qualitative and Quantitative Phase-Analysis of Undoped Titanium Dioxide and Chromium Doped Titanium Dioxide from Powder X-Ray Diffraction Data. *Indonesian Journal of Chemistry*, *18*, 486. https://doi.org/10.22146/ijc.28892

Tegus, O., Brück, E., Buschow, K. H. J., & de Boer, F. R. (2002). Transition-metal-based magnetic refrigerants for room-temperature applications. *Nature*, *415*(6868), 150–152. https://doi.org/10.1038/415150a

Tishin, A. M., &Spichkin, Y. I. (2003). *The Magnetocaloric Effect and its Applications*. CRC Press. https://doi.org/10.1201/9781420033373

Tran, H. B., Fukushima, T., Momida, H., Sato, K., Makino, Y., &Oguchi, T. (2022). Direct and inverse magnetocaloric effects in FeRh alloy. *Journal of Alloys and Compounds*, *926*, 166718. https://doi.org/10.1016/j.jallcom.2022.166718

Varga, R., Ryba, T., Vargova, Z., Saksl, K., Zhukova, V., & Zhukov, A. (2011). Magnetic and structural properties of Ni–Mn–Ga Heusler-type microwires. *ScriptaMaterialia*, *65*(8), 703–706. https://doi.org/10.1016/j.scriptamat.2011.07.018

Venkataraman, R. (2020). Semiconductor detectors1. In M. F. L'Annunziata (Ed.), *Handbook of Radioactivity Analysis (Fourth Edition)* (pp. 409–491). Academic Press. https://doi.org/10.1016/B978-0-12-814397-1.00004-2

Vinod, A., ArvindhaBabu, D., &Wuppulluri, M. (2024). A Short Review on the Evolution of Magnetocaloric La(Fe,Si)13 and Its Fabrication through Melt Spinning. *ACS Omega*, *9*(10), 11110–11128. https://doi.org/10.1021/acsomega.3c08622

Von Dreele, R. B., & Toby, B. H. (2012). X-Ray Powder Diffraction. In *Characterization of Materials* (pp. 1–23). John Wiley & Sons, Ltd. https://doi.org/10.1002/0471266965.com071.pub2

Vorobiov, S., Pylypenko, O., Bereznyak, Y., Pazukha, I., Cizmar, E., Orendac, M., &Komanicky, V. (2021). Magnetic properties, magnetoresistive, and magnetocaloric effects of AlCrFeCoNiCu thin-film high-entropy alloys prepared by the co-evaporation technique. *Applied Physics A*, *127*. https://doi.org/10.1007/s00339-020-04145-6

Wade, D. M., & Drake, D. J. (2019). *A Brief Review of Modern Uses of Scattering Techniques*. *77*.

Weiss, P., & Piccard, A. (1917). Le phénomènemagnétocalorique. *Journal de Physique Théorique et Appliquée*, *7*(1), 103–109. https://doi.org/10.1051/jphystap:019170070010300

Wen, G., Zheng, R., Zhang, X., Wang, W., Chen, J., & Wu, G. (2002). Magnetic entropy change in LaFe13−xSix intermetallic compounds. *Journal of Applied Physics*, *91*, 8537–8539. https://doi.org/10.1063/1.1448793

Whittig, L. D., &Allardice, W. R. (1986). X-Ray Diffraction Techniques. In *Methods of Soil Analysis* (pp. 331–362). John Wiley & Sons, Ltd. https://doi.org/10.2136/sssabookser5.1.2ed.c12

Winkler, R. (2003). *Spin-orbit Coupling Effects in Two-Dimensional Electron and Hole Systems*. Springer Science & Business Media.

Wu, K., Liu, C., Li, Q., Huo, J., Li, M., Chang, C., & Sun, Y. (2019). Magnetocaloric effect of $Fe_{25}Co_{25}Ni_{25}Mo_5P_{10}B_{10}$ high-entropy bulk metallic glass. *Journal of Magnetism and Magnetic Materials*, *489*, 165404. https://doi.org/10.1016/j.jmmm.2019.165404

Xian, L., Yu, J., Lin, W., Ke, S., Liu, C., Nie, X., Zhu, W., Wei, P., He, D., Zhao, W., & Zhang, Q. (2023). Preparation and magnetocaloric performance of $La(Fe,Co,Si)_{13}$ alloys with wide transition temperature range. *Intermetallics*, *154*, 107827. https://doi.org/10.1016/j.intermet.2023.107827

Xie, K., Song, X., Zhu, Y., Lv, W., & Sun, Z. (2004). Large magnetic entropy change in melt-spun $LaFe_{11.5}Si_{1.5}$ ribbons. *Journal of Physics D: Applied Physics*, *37*(22), 3063. https://doi.org/10.1088/0022-3727/37/22/001

Xuan, H. C., Wang, D. H., Zhang, C. L., Han, Z. D., Gu, B. X., & Du, Y. W. (2008). Boron's effect on martensitic transformation and magnetocaloric effect in $Ni_{43}Mn_{46}Sn_{11}B_x$alloys. *Applied Physics Letters*, *92*(10), 102503.

Xue, L., Shao, L., Luo, Q., & Shen, B. (2019). $Gd_{25}RE_{25}Co_{25}Al_{25}$ (RE = Tb, Dy and Ho) high-entropy glassy alloys with distinct spin-glass behavior and good magnetocaloric effect. *Journal of Alloys and Compounds*, *790*, 633–639. https://doi.org/10.1016/j.jallcom.2019.03.210

Yadav, K., Kaur, G., Sharma, M. K., & Mukherjee, K. (2020). Magnetocaloric effect and spin-phonon correlations in $RFe_{0.5}Cr_{0.5}O_3$ (R = Er and Yb) compounds. *Physics Letters A*, *384*(26), 126638. https://doi.org/10.1016/j.physleta.2020.126638

Yeh, J.-W., Chen, S.-K., Lin, S.-J., Gan, J.-Y., Chin, T.-S., Shun, T.-T., Tsau, C.-H., & Chang, S.-Y. (2004). Nanostructured High-Entropy Alloys with Multiple Principal Elements: Novel Alloy Design Concepts and Outcomes. *Advanced Engineering Materials*, *6*(5), 299–303. https://doi.org/10.1002/adem.200300567

YU, P., & Cardona, M. (2010). *Fundamentals of Semiconductors: Physics and Materials Properties*. Springer Science & Business Media.

Zach, R., Chajec, W., Tobola, J., Fruchart, D., Hlil, E.-K., Balli, M., & Wolfers, P. (2011). Magnetic Properties and Magnetocaloric Effect in Selected MM'X-Type (M, M' = 3d or 4d Metal, X = As, P, Ge) and $Mn_{1-x}T_xAs$-Type (T = 3d Metal) Intermetallics. *Solid State Phenomena*, *170*, 180–184. https://doi.org/10.4028/www.scientific.net/SSP.170.180

Zayak, A., Entel, P., Enkovaara, J., Ayuela, A., & Nieminen, R. (2003). A First-Principles Investigation of Phonon Softenings and Lattice Instabilities in the Shape-Memory System Ni2MnGa. *Physical Review B*, *68*. https://doi.org/10.1103/PhysRevB.68.132402

Zhang, L., Meng, J., Yao, F., Liu, X., Meng, J., & Zhang, H. (2018). Strong-correlated behavior of 4f electrons and 4f5d hybridization in PrO2. *Scientific Reports*, *8*(1), 15995. https://doi.org/10.1038/s41598-018-34336-4

Zhang, X., Fan, J., Xu, L., Hu, D., Zhang, W., & Zhu, Y. (2016). Magnetic and magnetocaloric properties of nanocrystalline $La_{0.5}Sr_{0.5}MnO_3$. *Ceramics International*, *42*(1, Part B), 1476–1481. https://doi.org/10.1016/j.ceramint.2015.09.093

Zhang, X., Qian, M., Zhang, Z., Wei, L., Geng, L., & Sun, J. (2016). Magnetostructural coupling and magnetocaloric effect in Ni-Mn-Ga-Cu microwires. *Applied Physics Letters*, *108*(5), 052401. https://doi.org/10.1063/1.4941232

Zhang, X., Zhang, H., Qian, M., &Geng, L. (2018). Enhanced magnetocaloric effect in Ni-Mn-Sn-Co alloys with two successive magnetostructural transformations. *Scientific Reports*, *8*(1), 8235. https://doi.org/10.1038/s41598-018-26564-5

Zhang, Y., Qin, F., Estévez, D., Franco, V., & Peng, H.-X. (2020). Structure, magnetic and magnetocaloric properties of Ni_2MnGa Heusler alloy nanowires. *Journal of Magnetism and Magnetic Materials*, *513*, 167100. https://doi.org/10.1016/j.jmmm.2020.167100

Zhang, Y., Wu, B., Guo, D., Wang, J., & Ren, Z. (2021). Magnetic properties and promising cryogenic magneto-caloric performances of $Gd_{20}Ho_{20}Tm_{20}Cu_{20}Ni_{20}$ amorphous ribbons*. *Chinese Physics B*, *30*(1), 017501. https://doi.org/10.1088/1674-1056/abc0d7

Zheng, X. Q., Xu, Z. Y., Zhang, B., Hu, F. X., & Shen, B. G. (2017). The normal and inverse magnetocaloric effect in RCu_2 (R=Tb, Dy, Ho, Er) compounds. *Journal of Magnetism and Magnetic Materials*, *421*, 448–452. https://doi.org/10.1016/j.jmmm.2016.08.048

Zheng, Z. G., Chen, X. L., Wang, H. Y., Da, S., Wang, G., Qiu, Z. G., Zeng, D. C., & Xia, Q. B. (2023). Giant magnetocaloric effects of MnNiSi-based high-entropy alloys near room temperature. *Journal of Alloys and Compounds*, *966*, 171483. https://doi.org/10.1016/j.jallcom.2023.171483

Zhou, X., Li, W., Kunkel, H. P., & Williams, G. (2004). A criterion for enhancing the giant magnetocaloric effect: (Ni–Mn–Ga)—a promising new system for magnetic refrigeration. *Journal of Physics: Condensed Matter*, *16*(6), L39. https://doi.org/10.1088/0953-8984/16/6/L02

Zong, S. T., & Long, Y. (2017). The influence of Cr and Ni on the character of magnetic phase transition in $LaFe_{11.52-x}M_xSi_{1.48}$ alloys. *AIP Advances*, *8*(4), 048101. https://doi.org/10.1063/1.4993658

Zverev, V., &Tishin, A. M. (2016). Magnetocaloric Effect: From Theory to Practice. In *Reference Module in Materials Science and Materials Engineering* (p. B9780128035818028137). Elsevier. https://doi.org/10.1016/B978-0-12-803581-8.02813-7

Zwerger, W. (2009). Itinerant Ferromagnetism with Ultra cold Atoms. *Science*, *325*(5947), 1507–1509. https://doi.org/10.1126/science.1179767

دراسة مقارنة للخصائص المغناطيسية للمواد المغناطيسية

إعداد:

نهال محمود عبد الحميد أبو عصبة

إشراف:

د.حسين السمامرة

ملخص:

ازداد الطلب على بديل لأنظمة التبريد التقليدية خلال فترة ارتفاع استهلاك الطاقة، والذي من المتوقع أن يتضاعف ثلاث مرات بحلول عام 2050. وهذا صحيح بشكل خاص نظراً لأن الثلاجات التقليدية تساهم في ثقب طبقة الأوزون. ومع ذلك، لا يزال البحث مستمرًا للحصول على أفضل المواد المغناطيسية والتغلب على المشكلات المتعلقة بالمواد مثل الثبات الميكانيكي أو التباطؤ أو قابلية التشكيل. تعرض هذه الدراسة الاتجاه الحالي للمواد المغناطيسية وتسلط الضوء على أفضل المركبات والسبائك التي حظيت بالاهتمام في السنوات الأخيرة. كما تقدم تحليلًا مقارنًا للخصائص المغناطيسية للمواد ذات الاتجاه الحالي وفقًا لشكلها الفيزيائي وطريقة تركيبها وعناصر المركبات ونسبها وتأثير إضافة بعض العناصر على تلك الخصائص ركّزت هذه الدراسة على الخصائص السائبة لتلك المواد. لفحص الخواص الهيكلية والمغناطيسية بالتفصيل، يمكن باستخدام تقنيات متقدمة مثل التحليل الطيفي لامتصاص الأشعة السينية وقياسات المجال المغناطيسي العالي وتشتت النيوترونات لأنها توفر معلومات موضعية وتركز على موقع معين داخل المادة.